



Experimental and numerical investigations of yield surface, texture, and deformation mechanisms in AA5754 over low to high temperatures and strain rates

Amit Pandey^{a,b,*}, Akhtar S. Khan^a, Eun-Young Kim^c, Shi-Hoon Choi^{c,*}, Thomas Gnäupel-Herold^d

^a Department of Mechanical Engineering, University of Maryland, Baltimore County, Baltimore, MD 21250, USA

^b Materials Science and Technology Division, Oak Ridge National Laboratory, Oak Ridge, TN 37831-6069, USA

^c Department of Materials Science and Metallurgical Engineering, Suncheon National University, Suncheon, Jeonnam 540-742, Republic of Korea

^d NIST Center for Neutron Research, Gaithersburg, MD 20899-8562, USA

ARTICLE INFO

Article history:

Received 20 April 2012

Received in final revised form 29 August 2012

Available online 27 September 2012

Keywords:

AA5754

Texture

Neutron diffraction

Simple shear

Dynamic loading

Strain rate sensitivity

Polycrystal model

ABSTRACT

The effects of strain rate and temperature on the yield and flow stress of AA5754 sheets are presented under uniaxial (tension and compression), dynamic (tension), and simple shear loading conditions. The present study investigates the anisotropic behavior of AA5754 sheets through experiments performed in the rolling (RD), 45° to rolling (DD), and transverse to rolling (TD) directions at room and elevated temperatures. The experimental results show that the strain rate sensitivity varied from negative at room temperature to positive at elevated temperatures (>150 °C), and the anisotropy was inversely proportional to the strain rate. Texture analysis was conducted on the specimens after uniaxial tension and simple shear deformation, using the neutron diffraction and electron back-scattered diffraction (EBSD) techniques. Rotation rate maps and orientation stability parameters, determined by the rate-sensitive model, were used to explain the kinematic stability of the initial texture components in AA5754 sheets during uniaxial tension and simple shear deformation. A visco-plastic self-consistent (VPSC) polycrystal model was used to simulate the evolution of the initial texture components in AA5754 sheets during uniaxial tension and simple shear deformation.

© 2012 Elsevier Ltd. All rights reserved.

1. Introduction

The increasing use of aluminum in the automotive industry is mainly governed by the need for lower fuel consumption, which requires reducing the weight of the vehicle, thus providing the most energy efficient solution (Cole and Sherman, 1995). The replacement of steel with aluminum decreases the weight by as much as 40% as a result of its high strength-to-weight ratio. In addition, other qualities of sheet aluminum alloys – (1) high formability in stamping while retaining strength, (2) uniform, smooth surface after forming, and (3) high quality finish – make them desirable materials for use in the automotive industry (Burger et al., 1995). Therefore, investigations of 5xxx series aluminum alloys have focused on

* Corresponding authors. Address: Department of Mechanical Engineering, University of Maryland, Baltimore County, Baltimore, MD 21250, USA (A. Pandey). Tel.: +1 81 61 750 3556; fax: +1 82 61 750 3550.

E-mail addresses: dramitpandey@gmail.com (A. Pandey), shihoon@suncheon.ac.kr (S.-H. Choi).

the Portevin-Le Chatelier (PLC) effect, strain rate sensitivity, strain hardening and texture evolution, since these factors affect the structural response during forming operations and in crash failure.

Uniaxial tension experiments have been carried out on 5xxx series alloys by several researches (Naka and Yoshida, 1999; Wagenhofer et al., 1999; Sarkar et al., 2001; Li and Ghosh, 2003; Clausen et al., 2004; Picu et al., 2005; Kang et al., 2006; Abedrabbo et al., 2007; Hadianfard et al., 2008; Khan and Baig, 2011). These studies concluded that the stress–strain curves show serrated flow behavior at lower temperatures. However, there was an absence of serrated flow and a decrease in flow stress at elevated temperatures. The former was due to DSA, while the latter can be attributed to the increase in the mobility of the solute atoms, which eliminates the serrated flow behavior. In addition, AA5754-O and AA5182 sheets softened at 121 and 93 °C, respectively, and there was a steady decrease in strain hardening and an increase in SRS with increased temperature (Abedrabbo et al., 2007). Picu et al. (2005) reported negative SRS for temperatures ranging from –100 to 80 °C, i.e., the DSA mechanism dominated the behavior in this temperature range. The work of Park and Niewczas (2008a) on AA5754 alloy revealed two kinds of flow instability, the PLC effect at room temperature and adiabatic deformation at –270 °C. Almost all uniaxial tension experiments are performed using hydraulic or screw-driven tensile testing systems, and the resultant strain measurements were obtained using an extensometer or machine displacement. However, Kang et al. (2006) used digital image correlation (DIC) to measure full field strain and the SEM topography image correlation technique was used to perform strain mapping to the grain level. Biaxial experiments were also performed by Iadicola et al. (2008) on AA5754-O sheet alloy, and stresses were measured using the X-ray diffraction method.

High strain rate tension experiments by Smerd et al. (2005) on AA5182 and AA5754 sheets, using a tension split Hopkinson bar (TSHB), showed that both alloys exhibited significant increases in ductility under a dynamic regime. A comprehensive study was recently performed by Khan et al. (2009,2010a,b) on high- and low-hardening Al alloys, and they reported that the small scale yield surfaces showed completely different behaviors with different proportions of isotropic and kinematic hardening. Uniaxial and biaxial compression experiments on sheet alloys were initially performed by Tozawa (1978) using a rectangular specimen by stacking and gluing the sheet material. However, recent studies by Boger et al. (2005) and Lou et al. (2007) developed a new technique for in-plane compression experiments for sheet materials. In this technique, two flat steel plates and a hydraulic cylinder system are used to stabilize the sheet sample, and the stress–strain curves are obtained after making corrections for the friction between sample surfaces and supporting plates. Bouvier et al. (2006b) performed proportional and non-proportional simple shear experiments on AA5182-O to study the monotonic responses and Bauschinger effect. They concluded that the strain hardening increased with monotonic deformation, and no work-hardening stagnation was observed during strain path reversal with a small Bauschinger effect. Recently various experiments and modeling on various alloys and in particular Al alloys were reported by Ghavam and Naghdabadi (2011), Khan and Liu (2012), Brahme et al. (2011), Hamelin et al. (2011), Luo et al. (2012) and Sung et al. (2010) and explained the deformation mechanism at various strain rates, loading history and temperatures. However, a comprehensive study on AA5754 sheets has not been conducted, and the temperature dependence of SRS under various loading conditions, such as uniaxial (tension and compression) and simple shear loading, has not been determined.

Texture measurements on AA5754 alloy have been reported by Park and Niewczas (2008b) using Cu K α radiation. (1 1 1) and (2 0 0) pole figures showed that the commercial strip cast (SC) material (both as-received and annealed) exhibited a typical rolling texture with the β -fiber extending from copper to the Brass texture components. In the case of a deformed specimen under tension in the rolling direction (RD) at 4.2 and a 300 K temperature range with an initial strain rate of 10^{-4} s^{-1} , the $\langle 111 \rangle$ and $\langle 100 \rangle$ are stable and meta-stable end orientations. Kang et al. (2006) used the electron back-scattering diffraction (EBSD) technique to determine the evolution of texture during tensile deformation, and revealed that there was no significant change in the volume fraction of eight primary texture components with increasing strain under tensile deformation. The results of the texture evolution of an AA5754 sheet were presented by Banovic et al. (2008) at different levels of strain under various strain paths (uniaxial tension, plane strain, and equibiaxial tension). It was found that similar deformation textures developed in the RD- and TD-oriented samples under each mode of deformation. However, the evolution of specific orientations depended upon the amount of deformation and the initial intensity of the texture components in the as-received material. While the basic observation of texture evolution in the AA5754 sheet was conducted for uniaxial, plane strain, and equibiaxial tension in the previous studies, absent from these works was the theoretical analysis explaining why the initial texture components depended upon the macroscopic deformation state. However, as far as we could ascertain, no study has yet documented the texture evolution and kinematic stability of initial texture components in the AA5xxx during simple shear deformation.

The main objective of the present study was to provide comprehensive experimental results for AA5754 sheets over a wide range of strain rates and temperatures using the same batch of material. This includes strain hardening, flow behavior and anisotropy under quasi-static, dynamic and simple shear loading conditions. The comprehensive experimental results provided the temperature dependence of SRS under various loading conditions such as uniaxial (tension and compression) and simple shear loading conditions. Texture measurements were performed to explain the evolution of the initial texture components in the RD- and TD-oriented samples during uniaxial tension and simple shear loading conditions. Moreover, a rate-sensitive polycrystal model (Choi et al., 2000a,b) was used to calculate the effect of the loading direction on the kinematic stability of initial texture components in the AA5754 sheet during uniaxial tension and simple shear deformation. A visco-plastic self-consistent (VPSC) polycrystal model (Molinari et al., 1987; Choi et al., 2000, 2007) was also used to simulate the evolution of the initial texture components in the AA5754 sheet during uniaxial tension and simple shear loading.

2. Experimental procedures

All specimens were machined from a commercial grade 1.4 mm-thick AA5754-O aluminum alloy sheet provided by General Motors Corporation (GMC).

2.1. Quasi-static tension and compression experiments

Sub-sized dogbone-shaped tension specimens were machined using ASTM-E8 with a gage length of 31.0 mm, a gage width of 6.4 mm, and thickness of 1.4 mm (sheet thickness). Tension experiments were conducted using a MTS tension/torsion servo-control loading frame. Two high elongation strain gages (KFEL-2-120-C1) were mounted in the loading and transverse-to-loading directions to obtain strains in both directions, and finally to measure the evolution of r -value (or plastic strain ratio) at each strain rate. Quasi-static compression specimens were prepared in three distinct directions, RD, TD, and DD, by bonding (using J-B Weld adhesive) three sheets that were 12.7 mm (0.5 in.) in length, 11.4 mm (0.45 in.) in gage width, and 4.2 mm (0.165 in.) in thickness. In addition, compression specimens were also prepared to perform experiments sheet-normal direction (ND). For high-temperature compression experiments, the stroke data was corrected using a blank test as explained by Khan et al. (2004).

2.2. Dynamic tension and simple shear experiments

The moderately high strain-rate tensile experiments were performed at room temperature using a direct tensile split Hopkinson bar (TSHB) apparatus (Fig. 1a). In addition, high-temperature dynamic experiments were performed using heating tape and gripping sections of bars that were covered by dry ice to avoid heating. Temperature was recorded using a thermocouple. The simple shear specimens were prepared by cutting the sheet into a number of rectangular pieces. These pieces were tested under simple shear loading with a gage length of 38.1 mm, a gage width of 6.0 mm, and a thickness of 1.4 mm (sheet thickness). These specimens were sheared along the gage length using a newly fabricated simple shear frame (Fig. 1b) in our laboratory, which was successfully used to perform experiments on AZ31 sheet alloy (Khan et al., 2011). This frame is very unique and simple by comparison with other designs (Bouvier et al., 2006a,b; Yoon et al., 2005) in that all parts of the frame are cylindrical, thereby making it easier to machine. Shear stress and strain were calculated from the corresponding load and actuator displacement values.

2.3. Texture measurement

Neutron diffraction measurements were carried out on the as-received specimen using the BT8 residual stress diffractometer at the Center for Neutron Research, National Institute of Standards and Technology (NIST), Gaithersburg, MD, USA. Due to the instrument design, with a variable take-off angle (Brand et al., 1997), the chosen wavelength was $\lambda = 0.2105$ nm, which made the reflections (1 1 1), (2 0 0), and (2 2 0) instrumentally accessible in the 2θ range from 46° to 116° . Specimens were prepared from the uniformly deformed gage section using an Isomet wafering blade and a Buehler Isomet low-speed saw. All grains in the specimen (gage section, about 0.3 cm^3) were illuminated by a neutron beam, and collectively contributed to the diffracted intensity.

The EBSD technique was used to analyze the evolution of texture in the RD- and TD-oriented samples during uniaxial tension and simple shear loading. The EBSD scan data were obtained after the occurrence of failure strain under uniaxial tension and finite deformation ($\gamma/\sqrt{3} = 20\%$) under simple shear loading, respectively. Deformed specimens were cut from the loading direction (LD)-width direction (WD) section. The EBSD specimens were prepared using colloidal silica as the polishing medium for the intermediate stage. The final specimens were prepared by electro-polishing in A2 electrolyte for the final stage. The measurement step size and the scanned area were $1.5 \mu\text{m}$ and $1000 \mu\text{m}$ (LD) \times $700 \mu\text{m}$ (WD), respectively. The EBSD data were analyzed using TSL software to evaluate the 3-D ODF.

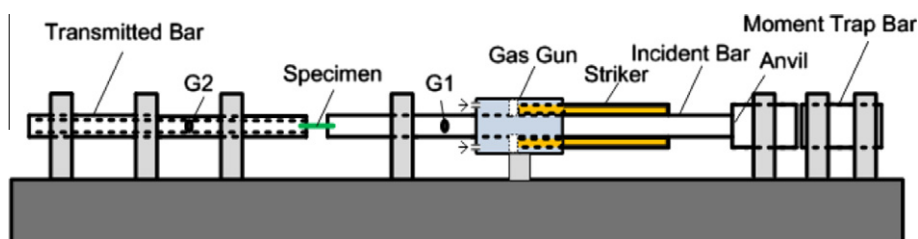


Fig. 1a. Schematic view of tensile split Hopkinson bar.

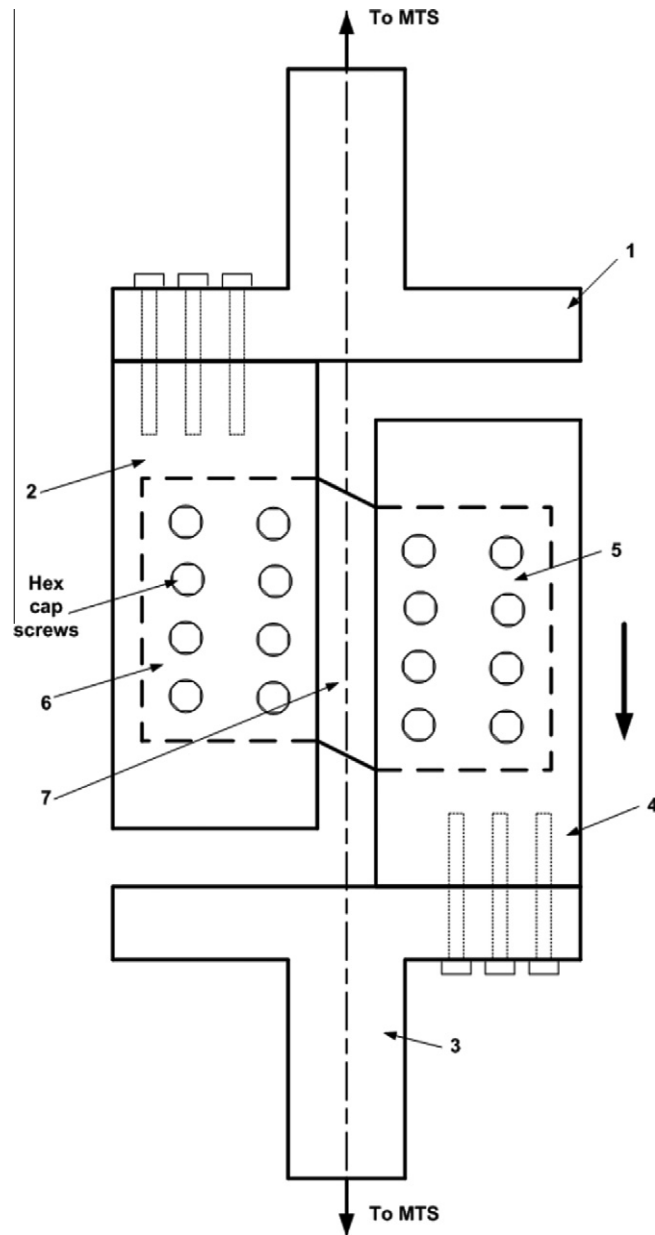


Fig. 1b. Schematic section view of the simple shear fixture (1) upper fixture, (2) upper middle fixture, (3) bottom fixture, (4) bottom middle fixture, (5) movable grip section of shear specimen, (6) fixed grip section of shear specimen, and (7) gage section of shear specimen.

3. Theoretical analysis

3.1. Orientation stability in Euler space

The stability of crystallographic orientations has been used to explain texture evolution during the plastic deformation of polycrystalline materials (Li, 2008; Arzaghi et al., 2009). However, a direct comparison of theoretical results with the experimental results of AA5xxx has not been conducted. A rate-sensitive polycrystal model (Choi et al., 2000) was used to predict the rotation rate map and orientation stability for the AA5754 sheet along the RD and TD during uniaxial tension and simple shear deformation. Uniaxial tension as a function of the r -value (R) and simple shear deformation with shear rate $\dot{\gamma}$ were imposed on FCC polycrystals, as defined by the following velocity gradient tensor in a rectangular reference system:

Table 1
Microscopic hardening coefficients for the VPSC polycrystal model.

Deformation mode	τ_0^z (MPa)	h_0 (MPa)	τ_{sat} (MPa)	a
{111} <110>	53	900	134	2.5

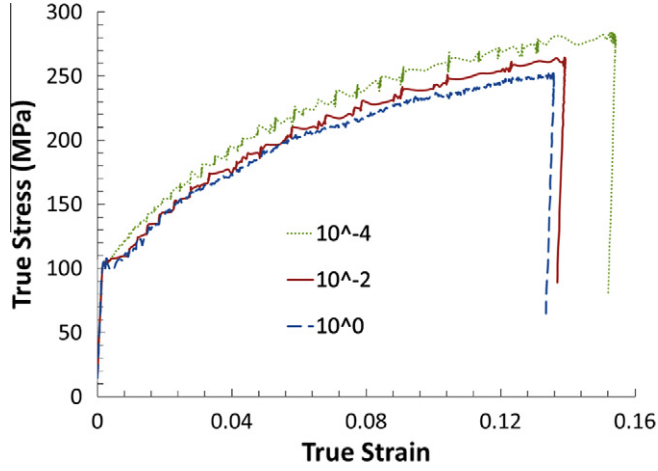


Fig. 1c. Tensile response in RD directions at room temperature.

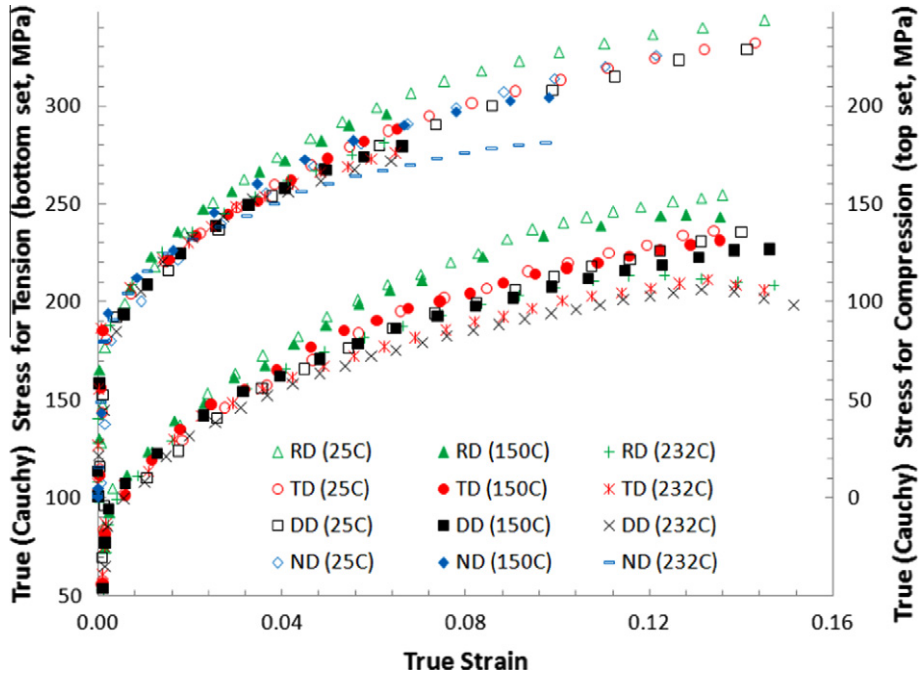


Fig. 2. Tension (bottom set) and compression (top set) responses at a strain rate of 10^0 s^{-1} , and at different temperatures and in different directions.

$$\mathbf{L} = \mathbf{D} = \mathbf{D}_{11} \begin{bmatrix} 1 & 0 & 0 \\ 0 & -R/(R+1) & 0 \\ 0 & 0 & -1/(R+1) \end{bmatrix} \quad \text{for uniaxial tension} \quad (1)$$

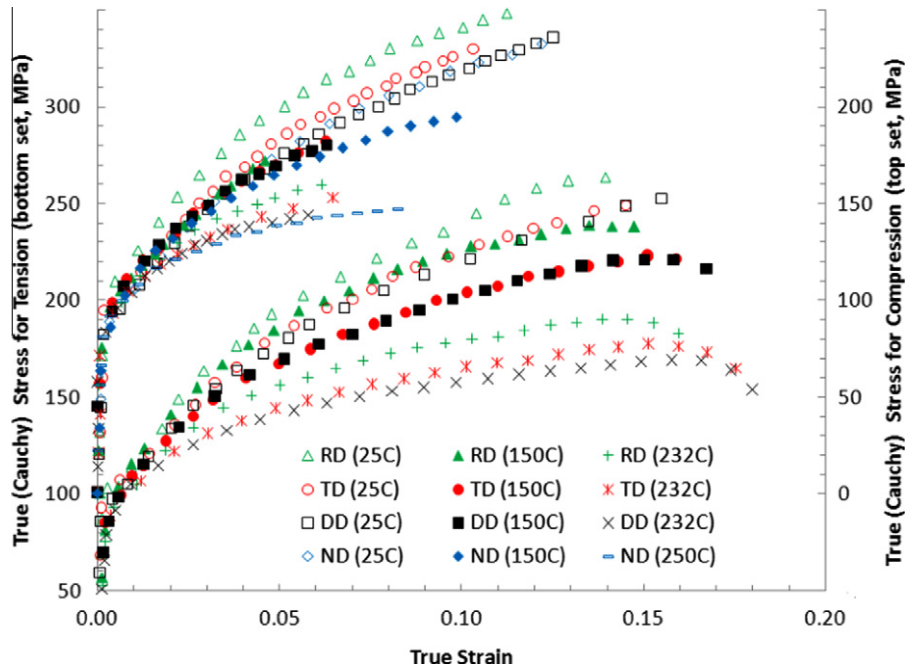


Fig. 3. Tension (bottom set) and compression (top set) responses at a strain rate of 10^{-2} s^{-1} , and at different temperatures and in different directions.

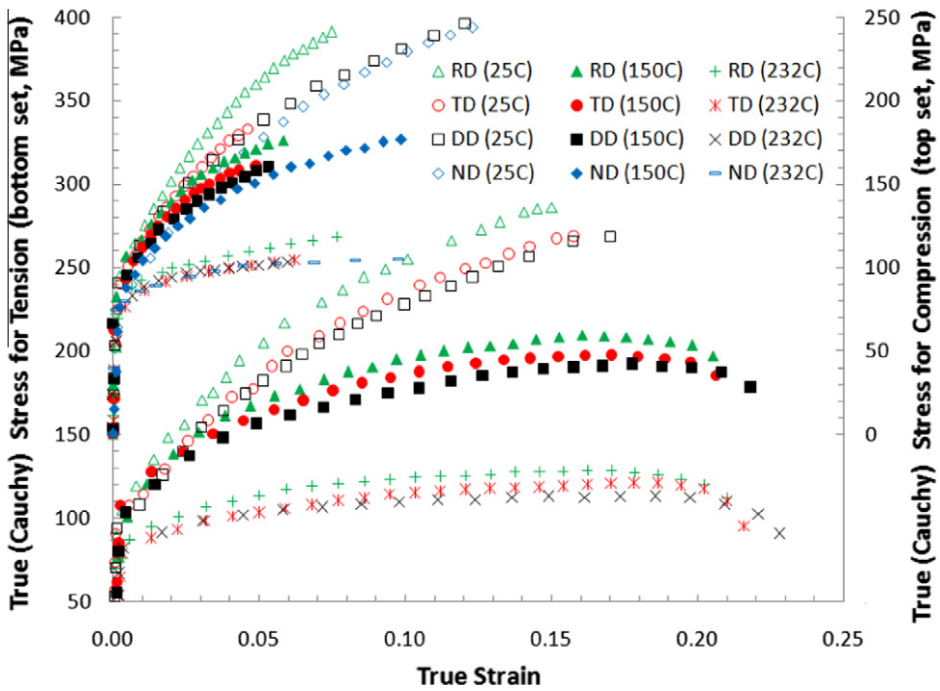


Fig. 4. Tension (bottom set) and compression (top set) responses at a strain rate of 10^{-4} s^{-1} , and at different temperatures and in different directions.

$$\mathbf{L} = \begin{bmatrix} 0 & \dot{\gamma} & 0 \\ 0 & 0 & 0 \\ 0 & 0 & 0 \end{bmatrix} \quad \text{for simple shear} \quad (2)$$

The deformation of rate-sensitive polycrystals is usually modeled by a power law relationship between the shear rate $\dot{\gamma}_s$ and the resolved shear stress τ^s on a slip system s :

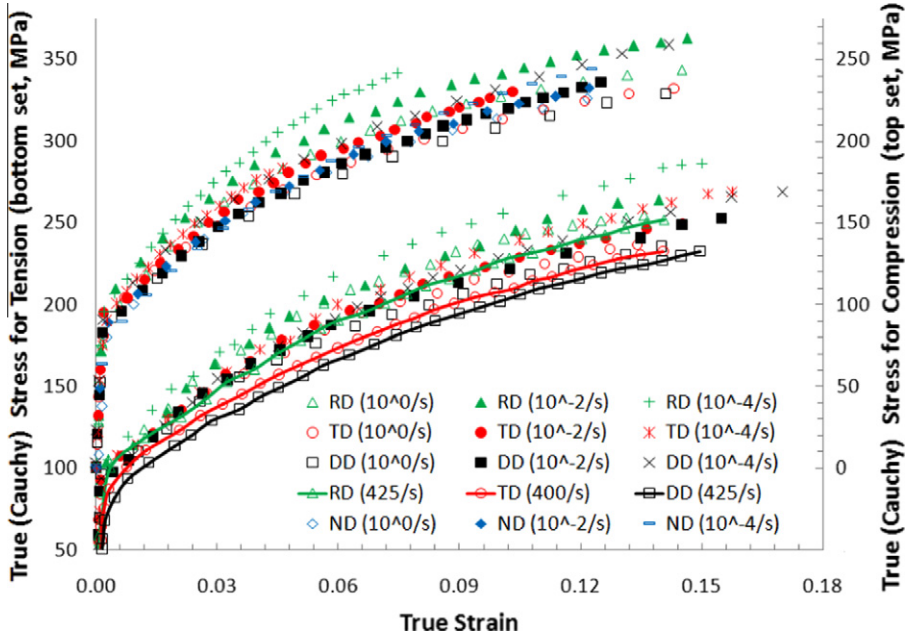


Fig. 5. Tension (bottom set) and compression (top set) responses at room temperature (25 °C), and at different strain rates and in different directions.

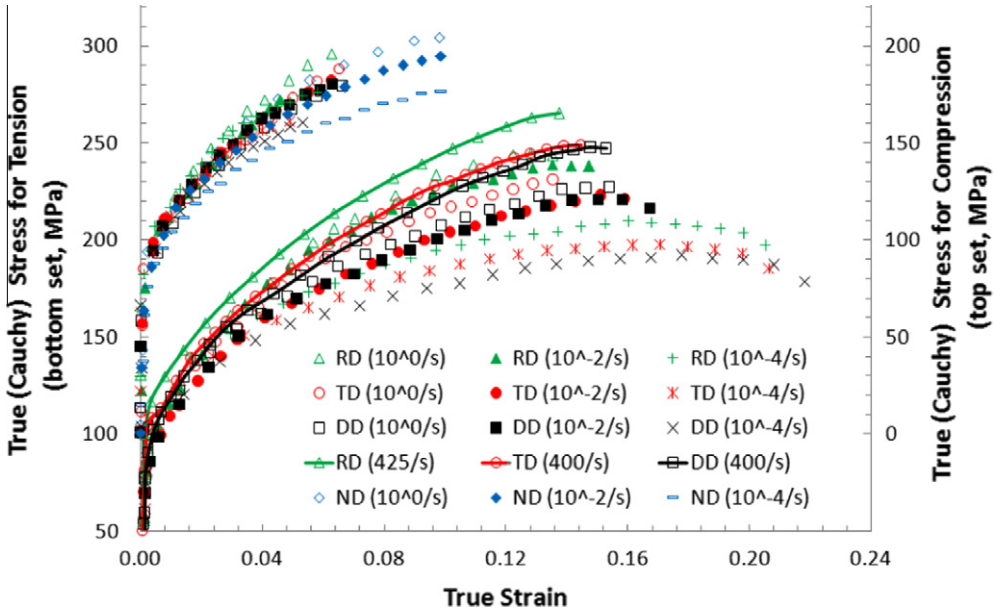


Fig. 6. Tension (bottom set) and compression (top set) responses at 150 °C, and at different strain rates and in different directions.

$$\tau^s = \tau_o \text{sgn}(\dot{\gamma}_s) \left| \frac{\dot{\gamma}_s}{\dot{\gamma}_o} \right|^p = \tau_o \frac{\dot{\gamma}_s}{\dot{\gamma}_o} \left| \frac{\dot{\gamma}_s}{\dot{\gamma}_o} \right|^{p-1} \quad (3)$$

where p ($=0.05$) is the rate sensitivity parameter, τ_o is a reference shear stress, and $\dot{\gamma}_o$ is a reference shear rate. The sign term in Eq. (3) means that the shear rate has the same sign as the resolved shear stress. The resolved shear stress is related to the Cauchy stress tensor σ_{ij} of the crystal, through the following relationship:

$$\tau^s = \sigma : \vec{b}^s \otimes \vec{n}^s = \sigma : \mathbf{m}^s \quad (4)$$

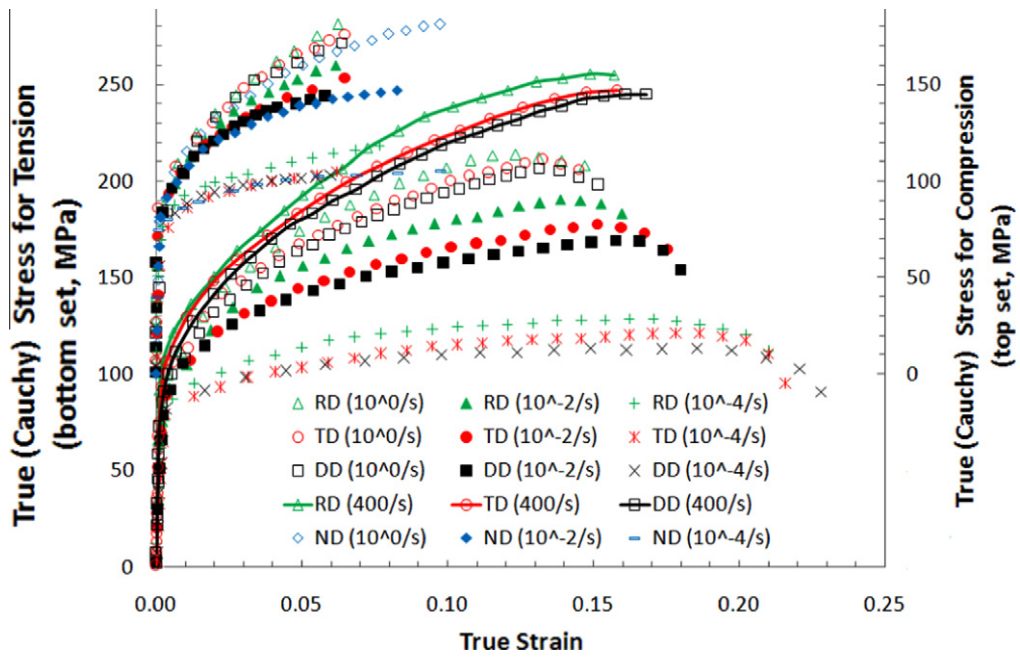


Fig. 7. Tension (bottom set) and compression (top set) responses at 232 °C, and at different strain rates and in different directions.

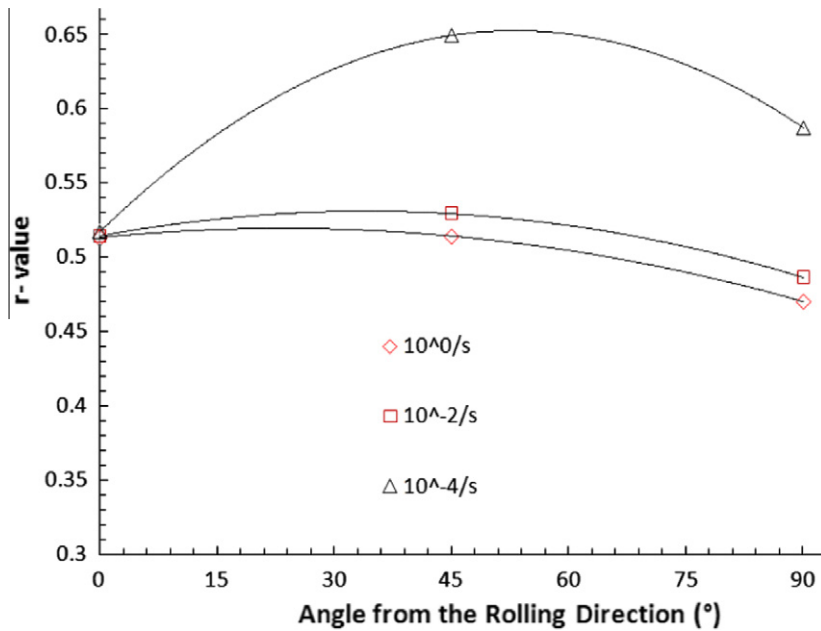


Fig. 8. R-values as a function of strain rates.

where the Schmid tensor $\mathbf{m}^s (= \vec{b}^s \otimes \vec{n}^s)$ is defined with the component of the unit vector n_j^s , which is normal to the slip plane, and the unit vector b_i^s , which is parallel to the slip direction of the slip system s . When the elastic deformation is ignored, the vectors n_j^s and b_i^s are orthogonal.

The lattice rotation rate, $\dot{\Omega}_{ij}$, with respect to the laboratory is given as follows:

$$\dot{\Omega}_{ij} = L_{ij} - \sum_s m_{ij}^s \dot{\gamma}_s \tag{5}$$

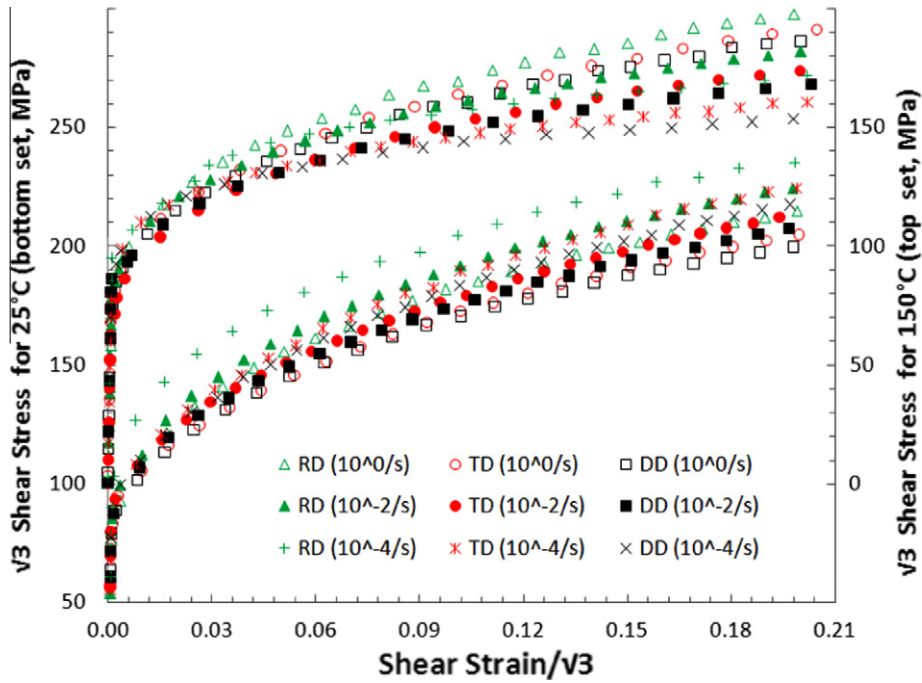


Fig. 9. Shear responses at temperatures of 25 °C (bottom set) and 150 °C (top set), and at different strain rates and in different directions.

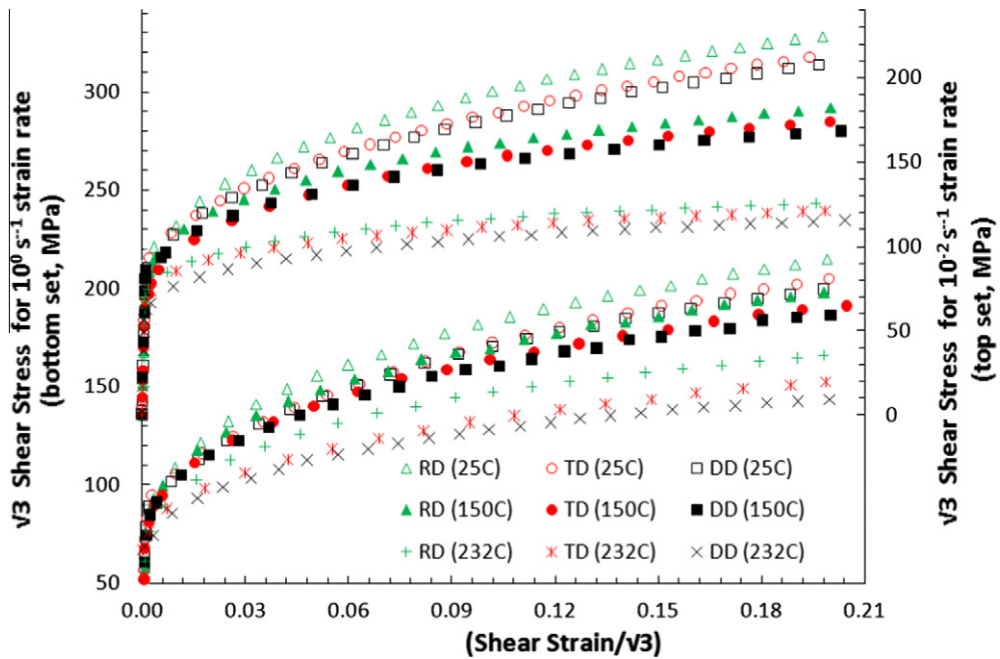


Fig. 10. Shear responses at strain rates of 10⁰ s⁻¹ (bottom set) and 10⁻² s⁻¹ (top set), and at different temperatures and in different directions.

The lattice rotation rate can be obtained from the prescribed velocity gradient tensor, L_{ij} , and the calculated shear rate, $\dot{\gamma}_s$. The Euler angles $(\varphi_1, \Phi, \varphi_2)$ of the individual orientations should be updated according to the lattice rotation rate, $\dot{g} = (\dot{\varphi}_1, \dot{\Phi}, \dot{\varphi}_2)$, as follows:

$$\begin{aligned}
 \dot{\varphi}_1 &= (\dot{\Omega}_{32} \sin \varphi_2 + \dot{\Omega}_{13} \cos \varphi_2) / \sin \Phi \\
 \dot{\Phi} &= \dot{\Omega}_{32} \cos \varphi_2 - \dot{\Omega}_{13} \sin \varphi_2 \\
 \dot{\varphi}_2 &= \dot{\Omega}_{21} - \dot{\varphi}_1 \cos \Phi
 \end{aligned}
 \tag{6}$$

The kinematic stability of an orientation can be estimated using two parameters. The first parameter is the condition for either convergence or divergence of an orientation in 3-D Euler space. The condition can be expressed by divergence of the rotation field, $\dot{\mathbf{g}} = (\dot{\varphi}_1, \dot{\Phi}, \dot{\varphi}_2)$, as follows:

$$\text{div } \dot{\mathbf{g}} = \frac{\partial \dot{\varphi}_1}{\partial \varphi_1} + \frac{\partial \dot{\Phi}}{\partial \Phi} + \frac{\partial \dot{\varphi}_2}{\partial \varphi_2}
 \tag{7}$$

The conditions for convergence and divergence are $\text{div } \dot{\mathbf{g}} < 0$ and $\text{div } \dot{\mathbf{g}} > 0$, respectively. $\text{Div } \dot{\mathbf{g}} < 0$ indicates that more orientations around \mathbf{g} rotate toward \mathbf{g} . The second parameter is the relative magnitude of the lattice rotation rate of the orientation in 3-D Euler space. The stability parameter, Q , can be expressed in terms of the lattice rotation rate (Choi et al., 2009):

$$Q = \ln \left(\frac{\dot{\epsilon}_{eq}}{|\dot{\Omega}|} \right) = \ln \left(\frac{\dot{\epsilon}_{eq}}{[\dot{\Omega}_{32}^2 + \dot{\Omega}_{13}^2 + \dot{\Omega}_{21}^2]^{1/2}} \right)
 \tag{8}$$

where $\dot{\epsilon}_{eq}$ is the von Mises equivalent strain rate for the deformation mode of interest. In the present study, $\dot{\epsilon}_{eq}$ with $D_{11} = 0.01 \text{ s}^{-1}$ and $\dot{\gamma} = 0.01 \text{ s}^{-1}$ in Eqs. (1) and (2) was imposed on polycrystalline materials. Kinematically stable orientations have high values of Q , compared with unstable orientations. However, when $|\dot{\Omega}|$ is equal to zero, this parameter can be infinity. Therefore, in order to derive a persistent form that could be used for any orientation, the stability parameter was modified as follows:

$$Q = \ln \left(\frac{\dot{\epsilon}_{eq}}{(|\dot{\Omega}| + \dot{\epsilon}_{eq} / \exp(5))} \right)
 \tag{9}$$

The $\exp(5)$ in Eq. (5) was selected so that the maximum value of Q would not be exceed 5.

3.2. Texture simulation

In order to simulate the texture evolution of the AA5754 sheets during uniaxial tension and simple shear deformation, the VPSC polycrystal model (Molinari et al., 1987; Choi et al., 2000a,b, 2007) was used. Using the Homogeneous Equivalent

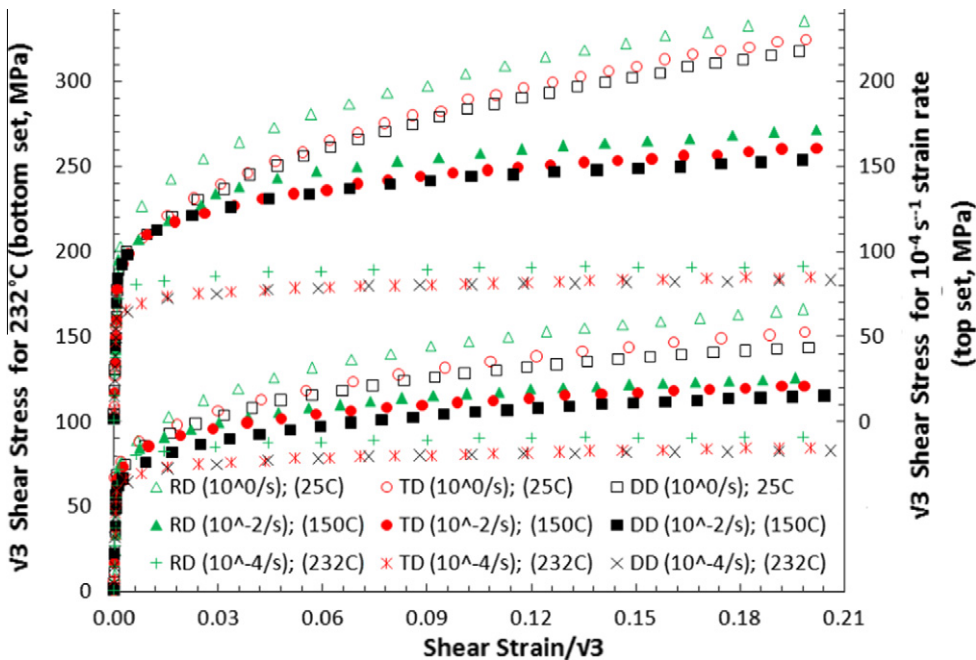


Fig. 11. Shear responses at 232 °C (bottom set) at different strain rates and in different directions, and shear responses at 10^{-4} s^{-1} (top set) at different temperatures and in different directions.

Matrix (HEM) concept with 1-site approximation, the VPSC scheme provides the interaction law between a grain and the matrix,

$$\sigma^g - \bar{\sigma} = (\Gamma^{gg'}^{-1} + A_o) : (D^g - \bar{D}) \tag{10}$$

where $\bar{\sigma}$ and \bar{D} are the deviatoric stress and strain rate for the matrix. The effect of grain shape can be taken into account by the interaction, tensor Γ , between single crystals g and g' , with components that depend only on shape. The tensor Γ can be obtained by integration of the symmetric part of the second derivative of the Green function. In the calculation of the interaction tensor, A_o , isotropic behavior of the HEM was assumed. Isotropic denomination does not imply an assumption of isotropic macroscopic response, but only refers to the way in which the grain–matrix interaction is treated. Self and latent hardening on a slip system can be considered by a suitable evolution of the reference shear stress, τ_o^i . The method proposed by Kalidindi et al. (1992) applied in this study, uses the following hardening law:

$$\dot{\tau}_o^i = \sum_j H^{ij} |\dot{\gamma}^j| \quad i, j = 1, \dots, n \tag{11}$$

$$H^{ij} = q^{ij} h_o \left(1 - \frac{\tau_o^i}{\tau_{sat}^i} \right)^a \tag{12}$$

where n is the total number of slip systems in Eq. (9), and H^{ij} is the $(n \times n)$ hardening matrix. In this study, 12 slip systems $(\{111\} \langle 110 \rangle)$ were considered. Here, it is assumed that the self-hardening term (diagonal term of q^{ij}) equals the latent hardening term (off-diagonal term of q^{ij}), i.e. $(=1)$. The hardening parameters, listed in Table 1, were determined by fitting the experimental flow stress to the macroscopic flow curve of the AA5754 sheet under uniaxial tension along the RD at a strain rate of 10^0 s^{-1} and at room temperature. For uniaxial tension simulations, macroscopic deformation states were changed iteratively until the macroscopic stress state converged toward the uniaxial stress state.

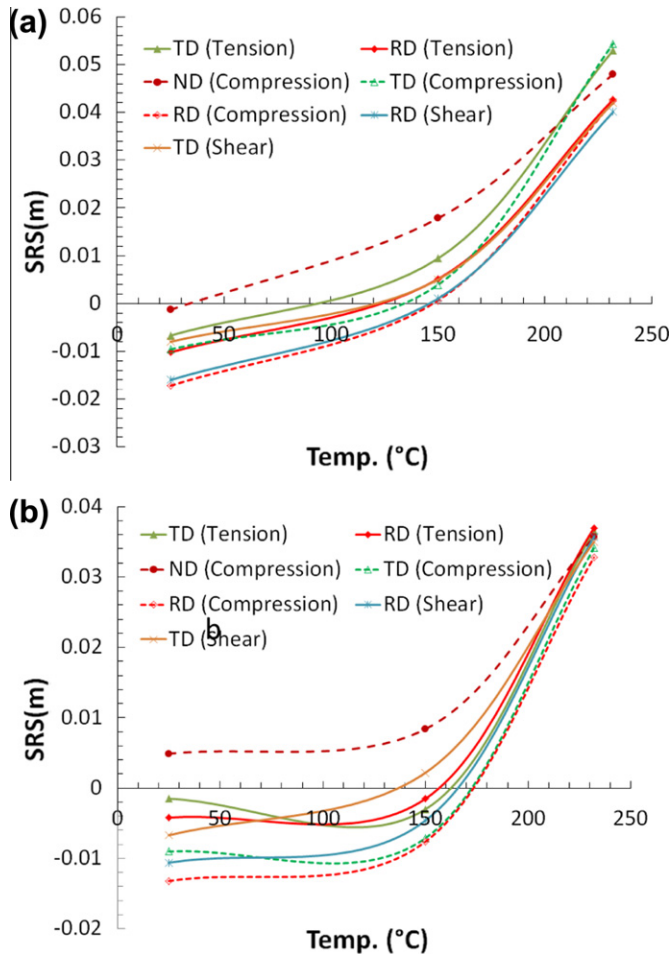


Fig. 12. Plot of strain rate sensitivity (SRS) with temperature at (a) 2% and (b) 5% strain.

The self-consistent model relies on the fact that A_0 is calculated so that

$$\bar{\sigma} = \langle \sigma^g \rangle \quad \text{and} \quad \bar{D} = \langle D^g \rangle \quad (13)$$

where $\langle \rangle$ means the arithmetic volume average over the polycrystal aggregate.

4. Results and discussion

4.1. Stress–strain responses and anisotropy

Fig. 1c shows the serrated yielding behavior also known as the PLC effect which is mainly caused either due to the interaction of dislocation–solute atom or dislocation–precipitate. The PLC effect results in plastic instability due to strain localizations, and can be observed as a serrated flow in perfectly plastic regions of stress–strain curves. The study performed by Wen and Morris (2003) on three types of 5000 series alloy supports the dislocation–solute model where serrated yielding is caused by Mg and discussed its dependency on temperature and the strain rate. As seen in Fig. 1c where there is an increase in serrated behavior with a decrease in the strain rate (or increase in temperature). Wen and Morris (2003) also observed a decrease in the magnitude of the serrations and a delay serrated phenomenon at lower temperatures. Figs. 2–4 show the effect of strain rate at different temperatures and directions under uniaxial tension and compression loadings, and reveal its effect on anisotropy and flow stress. It is clear that both yield and flow stresses were inversely proportional to temperature and directly proportional to strain rate. In addition, the descending order of strength was in the RD, TD, and DD directions. The stress–strain responses in the ND direction (through thickness) were also comparable to the DD direction (in-plane). The yield and flow stresses decreased as temperature increased, and this decrease was more pronounced at 10^{-4} s^{-1} . The plots of stress–strain responses shown in Figs. 5–7 disclose the effect of temperature at different quasi-static and dynamic strain rates and directions. This decrease in flow stress with the increase in strain rate, also known as negative strain rate sensitivity is an effect of dynamic strain ageing (DSA). Similar, behavior was reported by Wen and Morris (2003)

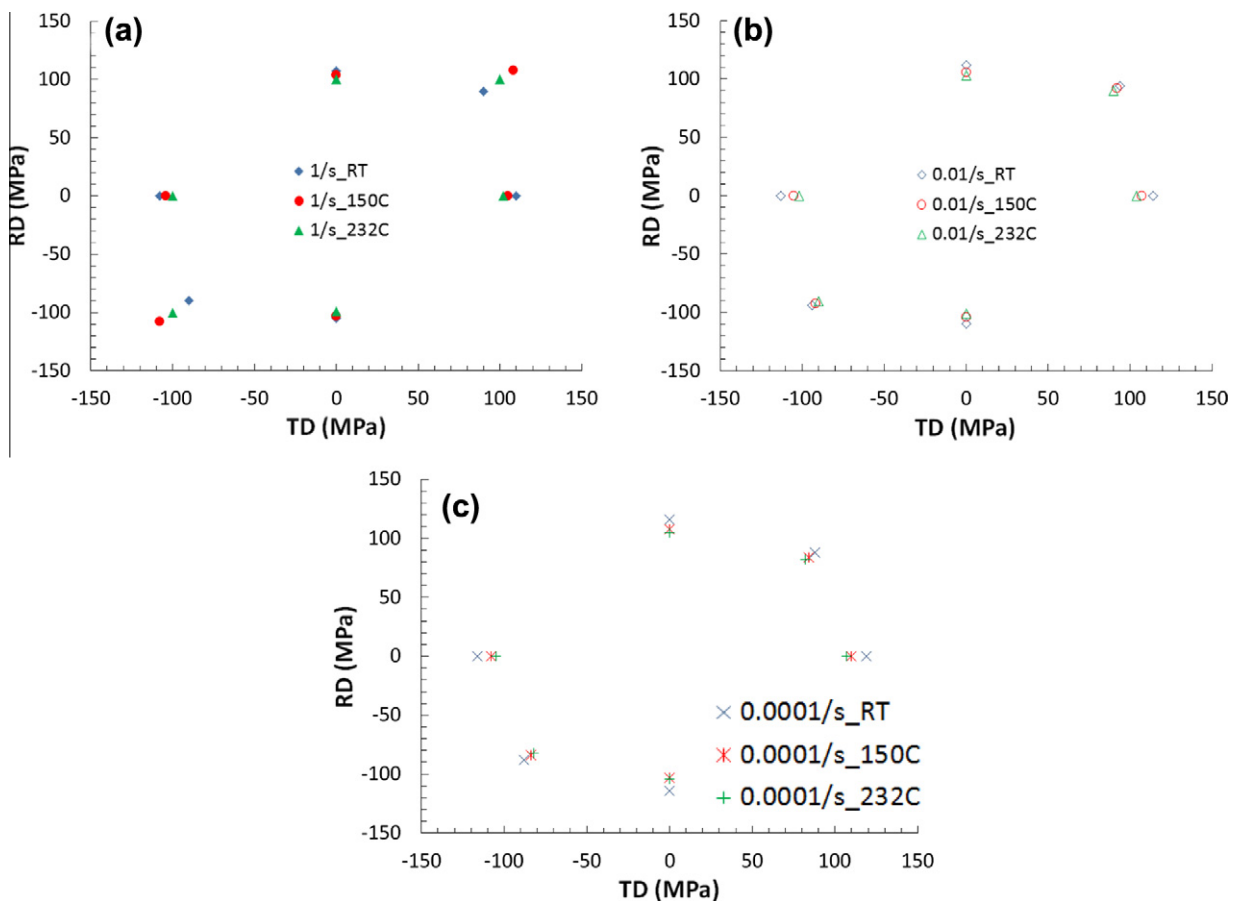


Fig. 13. (a–c) Plot of yield stresses at different strain rates and temperatures at 0.2% strain (the bi-axial tension and compression yield stresses were calculated by assuming pressure insensitivity).

for 5000 series aluminum alloys and was attributed to an increase in the velocity of mobile dislocations with an increase in the strain rate. DSA leads to negative strain rate sensitivity (SRS) at lower temperatures, when the mobile dislocations and solute atoms have comparable mobility. At high strain rates, when the average arrest time is short, the clusters of mobile solute atoms are too small to increase the strength of an obstacle. As a result, serrated flow behavior is not evident in the stress–strain responses. The negative SRS is also undesirable in industrial processing as it leads to poor material formability.

Like most metallic alloys, there was a decrease in flow stress and hardening and an increase in failure strain with elevated temperatures. The temperature sensitivity increased at a slow strain rate, which emphasizes the shifting balance between dynamic recovery (large temperature effect at low strain rate; strain rate in line with dislocation mobility and annihilation rate) and strain hardening (increase in dislocation density and entanglement). The strain rate sensitivity changed from negative to positive at 150 °C, and the transition temperature was dependent on strain, because at higher temperatures, solute atoms move more rapidly and the dislocation climb becomes easier. The climb and thermally activated glide lead to a higher SRS value as the temperature increases. This overshadows the dynamic recovery increase in temperature (indicated by higher elongations). The yield and flow stresses were highest for specimens oriented along the RD and lowest in specimens oriented along the DD, and for each strain rate and temperature the strength of specimens oriented along the TD approximated that of specimens oriented along the DD. Fig. 8 shows the variation of r -values at room temperature with an angle from the RD at various strain rates. The material showed strong anisotropy in the DD direction and was highest at a strain rate of 10^{-4} s^{-1} . Also, there was a gradual decrease in r -value for each loading direction as the strain rate increased. We knew that discontinuous yield significantly affects the r -value when an effective offset is imposed on the width strain measurement during a sheet tensile test (Hance, 2005). The average yield point (YP) elongations at strain rates of 10^{-4} s^{-1} , 10^{-2} s^{-1} , and 10^0 s^{-1} were 0.0038, 0.0072, and 0.0074. Therefore, it seems that the low level of YP elongation cannot sufficiently explain the significant change in r -value. In the future, more systematic research is required on this point.

It is also evident from Figs. 9–11 that equivalent shear yield stress was closer to yield stress under tension and compression response stress–strain at all strain rates and temperatures. However, the stress–strain curves showed different values for the hardening rate as compared with tension and compression in all directions, temperatures and strain rates. The stress–strain curves under shear loading also showed negative SRS at room temperature and positive SRS at elevated temperatures.

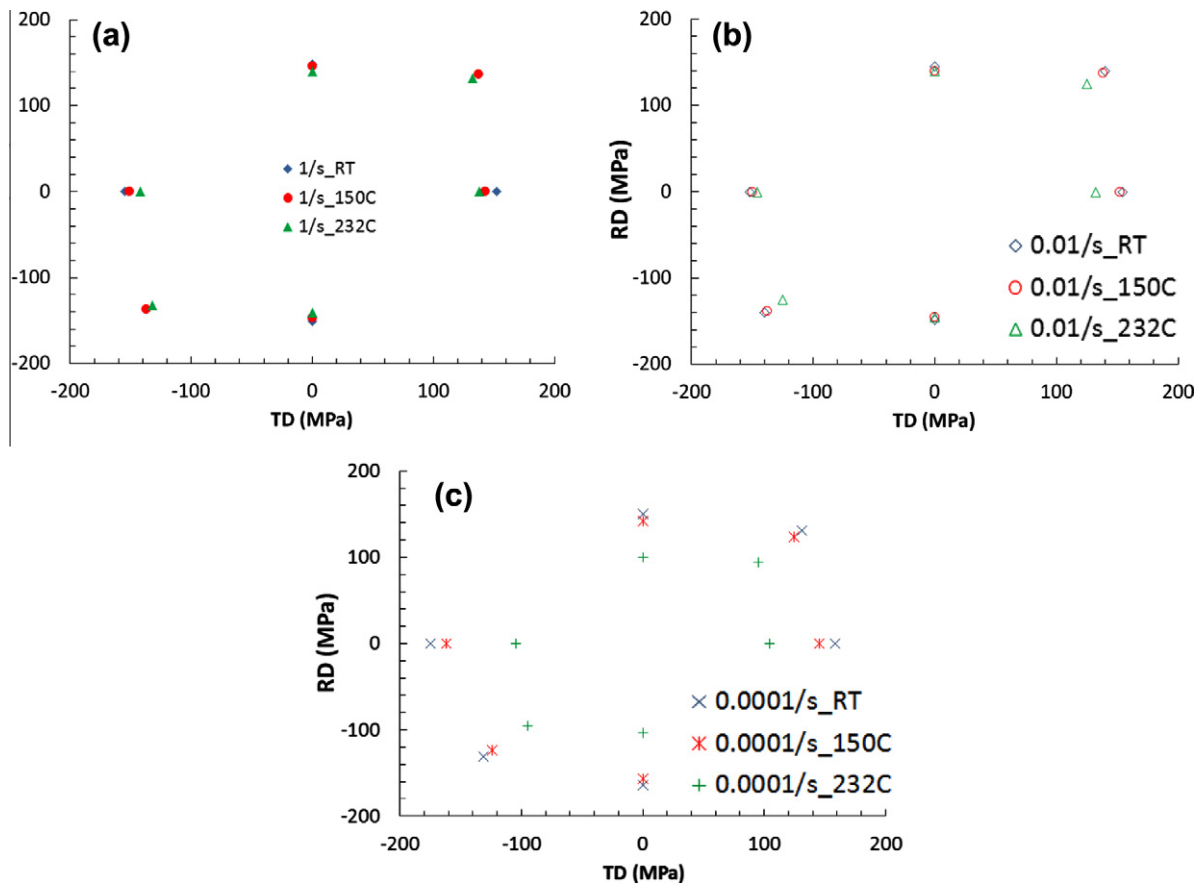


Fig. 14. (a–c) Plot of yield stresses at different strain rates and temperatures at 2% strain (the bi-axial tension and compression yield stresses were calculated by assuming pressure insensitivity).

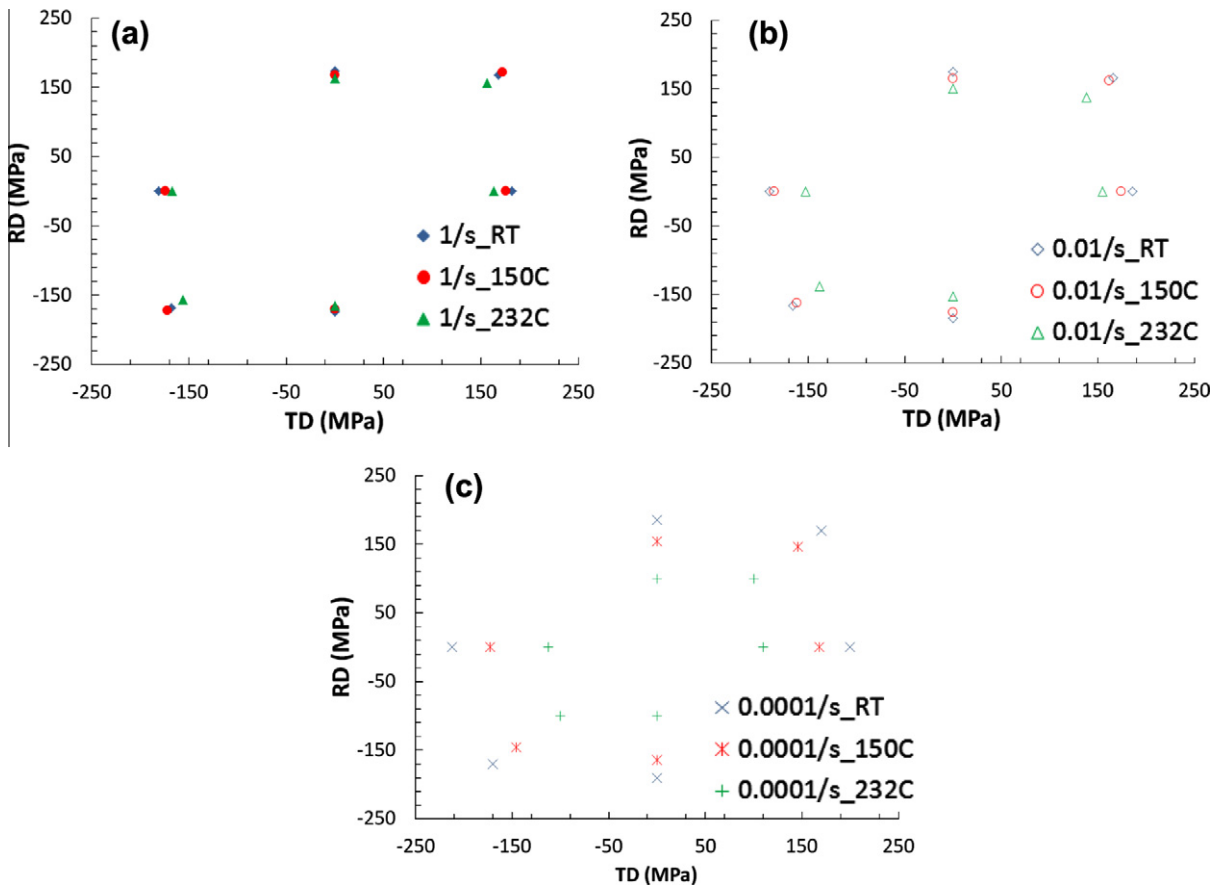


Fig. 15. (a–c) Plot of yield stresses at different strain rates and temperatures at 5% strain (the bi-axial tension and compression yield stresses were calculated by assuming pressure insensitivity).

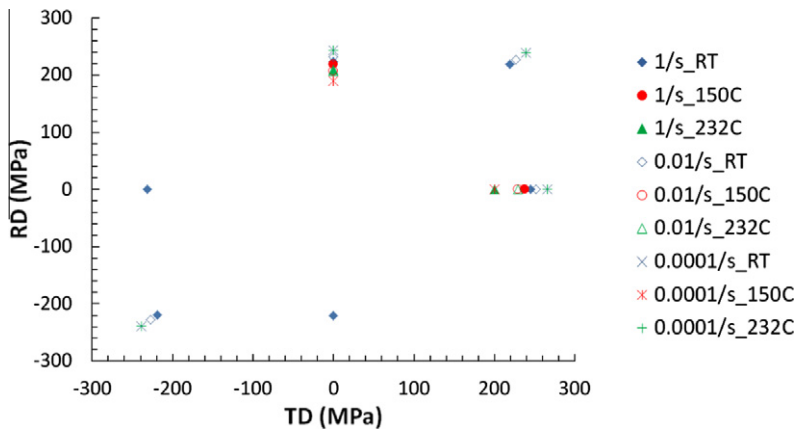


Fig. 16. Plot of yield stresses at different strain rates and temperatures at 10% strain (the bi-axial tension and compression yield stresses were calculated by assuming pressure insensitivity).

4.2. Strain rate sensitivity (SRS) and yield surfaces

It is clear from Fig. 12(a) and (b) that the AA5754 sheet showed negative and positive SRS at room and elevated temperatures (>200 °C), respectively. The transition temperature at which SRS changed from negative to positive was approximately 150 °C. It should be noted that the transition temperature of SRS was significantly dependent on the loading direction

under simple shear loading. The RD-oriented sample had a higher transition temperature than the TD-oriented sample. The plot also suggests that there was an increase in SRS with plastic strain. A study done by Khan and Baig (2011) on AA5182-O showed a similar SRS trend with temperature and the transition temperature of 120 °C.

Figs. 13–16 show plots of the flow stresses determined at 0.2, 2, 5, and 10% plastic strains under various strain rates, temperatures and loading conditions. The bi-axial tension and compressive stresses plotted in Figs. 13–16 were calculated by assuming that the material was pressure-insensitive and that bi-axial stresses under tension and compression were the same. Therefore, bi-axial tension stresses in the RD-TD plane equaled compression in the ND direction, and vice versa. These figures can be used to determine the coefficients of phenomenological yield function for AA5754 sheets under the various temperature and strain rate conditions.

Khan and Baig (2011) performed a 2-D plot of Barlat’s YLD96 yield function along with experimental responses at room temperature, and reported the change in the shape of the yield surfaces as compared with a von-Mises yield surface.

4.3. Texture evolution

4.3.1. Experiments observations

Fig. 17 shows the (1 1 1) pole figure and φ_2 sections of ODF of the as-received specimen, measured using the neutron diffraction technique. Triclinic sample symmetry was considered during ODF analysis and was compared with the results of the texture evolution of the deformed specimens, in particular, that produced by the simple shear deformation. The texture of the as-received specimen exhibited orthorhombic sample symmetry. Initial texture components could be characterized as rolling texture (Brass{011} <211>, Copper{112} <111>, S{123} <634>) and annealing texture (Cube{001} <100>) components, which are typical in FCC metals.

Fig. 18(a) shows the texture of the deformed specimen oriented along the RD after uniaxial tension at a strain rate of 10^{-4} s^{-1} and room temperature, as measured using the EBSD technique. Because the LD was parallel to the RD, this specimen was denoted as follows: LD//RD. Open symbols on the ODF sections represent the Euler angles of the initial texture components in the LD//RD specimen. Since the texture of the uniaxial tension specimen exhibited orthorhombic sample symmetry, φ_1 was confined to 90°. Texture analysis on the ODF sections indicated that the Copper and Cube components were relatively stable under uniaxial tension, compared to the Brass and S. Fig. 18(b) shows the texture of the LD//RD specimen deformed by uniaxial tension at a strain rate of 10^0 s^{-1} and room temperature. It was clear that there was little change in texture the

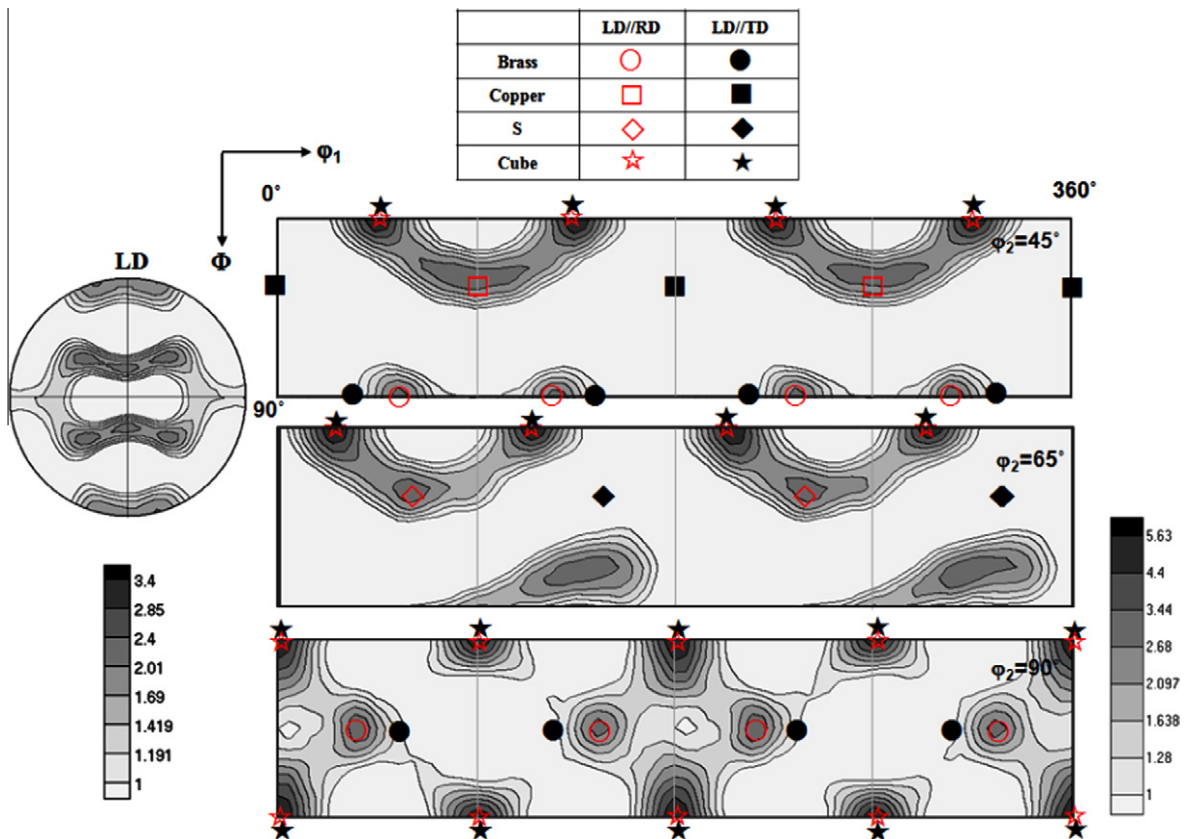


Fig. 17. (1 1 1) Pole figure and φ_2 sections of ODF of the as-received specimen, measured using the neutron diffraction technique.

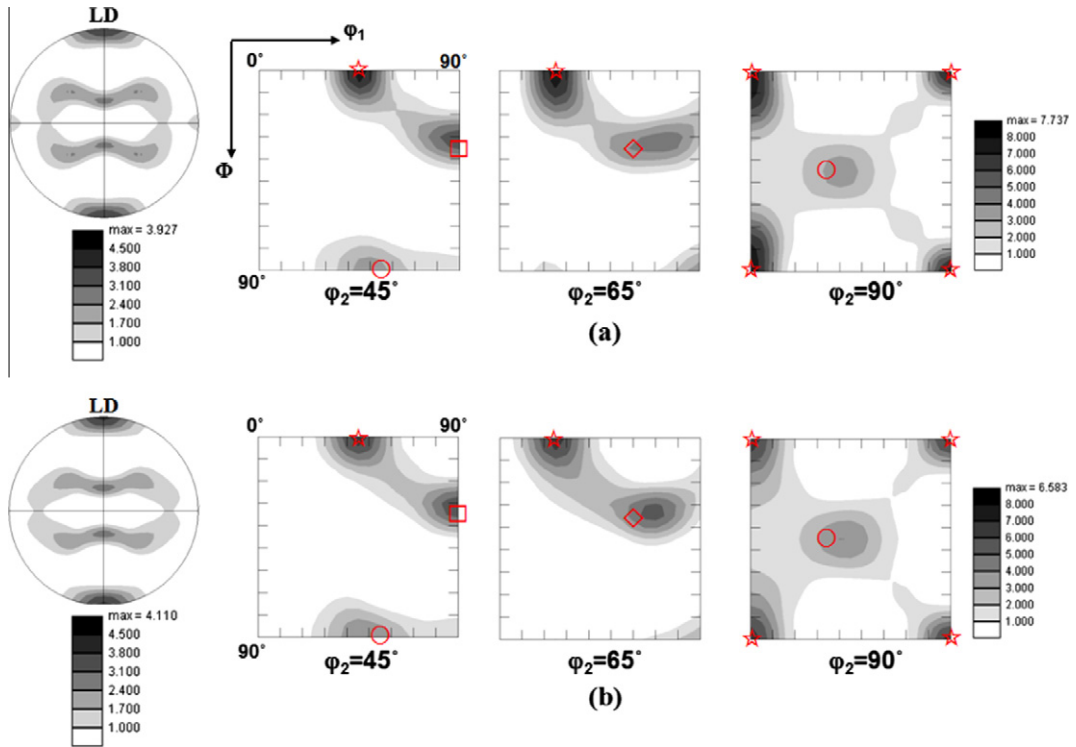


Fig. 18. (1 1 1) Pole figures and ϕ_2 sections of ODF of the deformed specimens after deformation under uniaxial tension along the RD (a) at a strain rate of 10^{-4} s^{-1} at room temperature and (b) at a strain rate of 10^0 s^{-1} at room temperature.

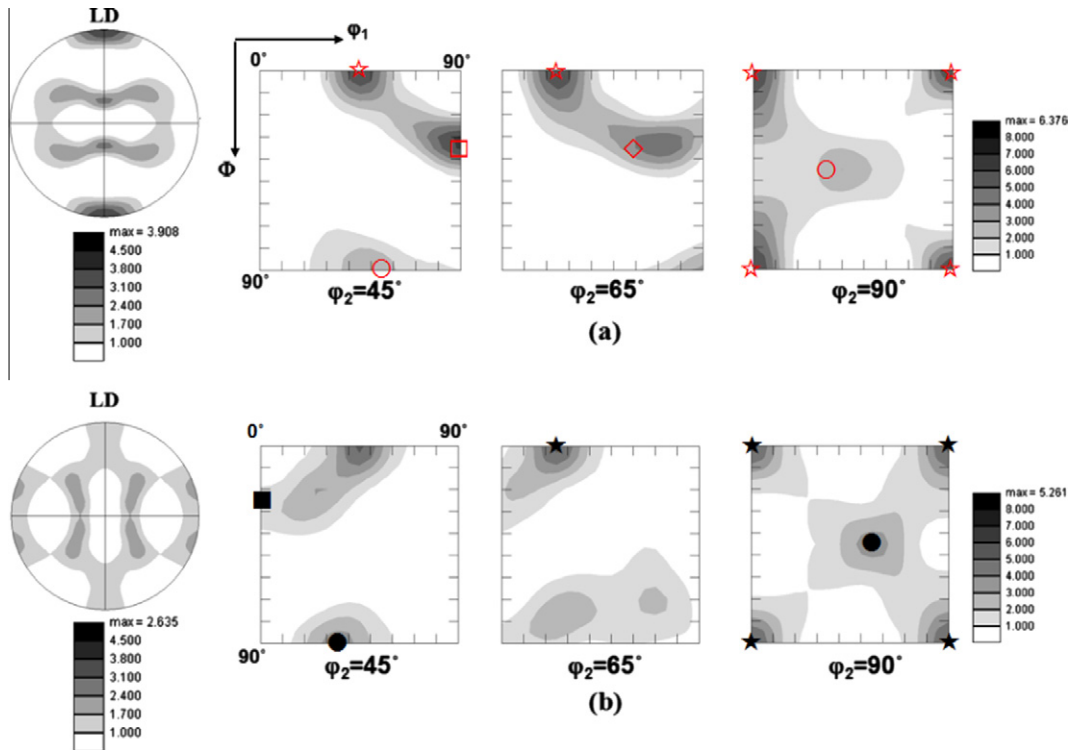


Fig. 19. (1 1 1) Pole figures and ϕ_2 sections of ODF of the deformed specimens after deformation under uniaxial tension along the RD (a) at a strain rate of 10^{-4} s^{-1} at 232° C and along the TD (b) at a strain rate of 10^0 s^{-1} at room temperature.

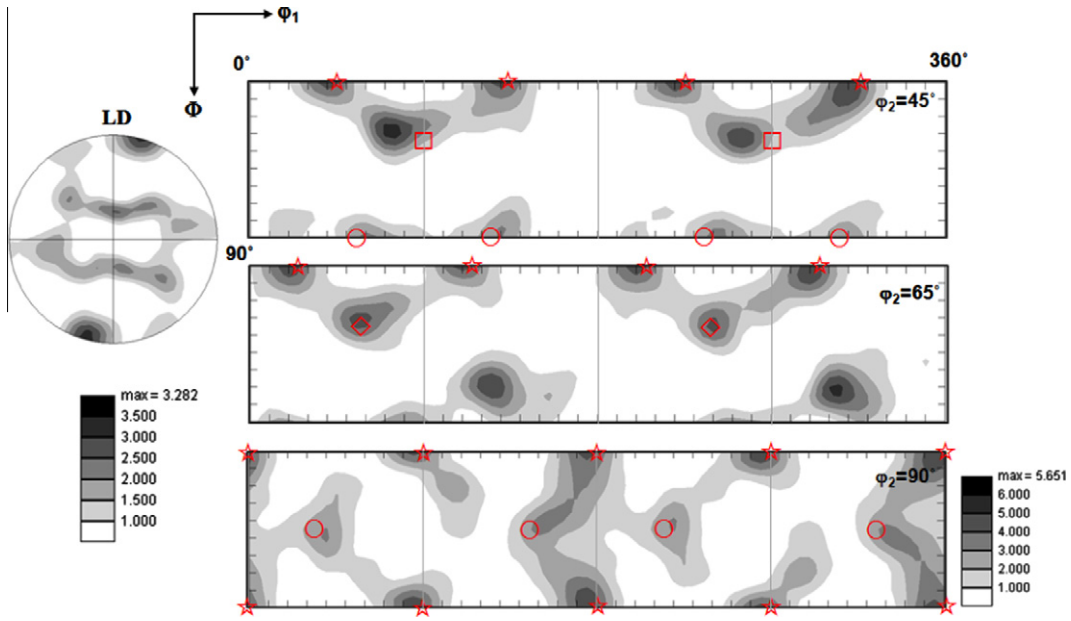


Fig. 20. (1 1 1) Pole figures and ϕ_2 sections of ODF of deformed specimen after deformation ($\gamma/\sqrt{3} = 20\%$) under simple shear loading along the RD at a strain rate of 10^{-4} s^{-1} and room temperature.

LD//RD specimen with strain rate at room temperature. Although not shown in the present paper, similar dependency of the strain rate was observed in the specimens oriented along DD (LD//DD) and the specimens oriented along TD (LD//TD) after uniaxial tension. Fig. 19(a) shows the texture of the LD//RD specimen deformed by uniaxial tension at a strain rate of 10^{-4} s^{-1} and 232 °C. A comparison between Fig. 18(b) and Fig. 19(a) reveals that a temperature increase from room temperature to 232 °C did not significantly affect the texture evolution in the LD//RD specimen during uniaxial tension. Texture evolution results during uniaxial tension were also reported by Park and Niewczas (2008b), and the evolution of texture was found to be independent of temperature. Fig. 19(b) shows the texture of the LD//TD specimen deformed by uniaxial tension at a strain rate of 10^0 s^{-1} and room temperature. The dark solid symbols on the ODF sections represent the Euler angles of

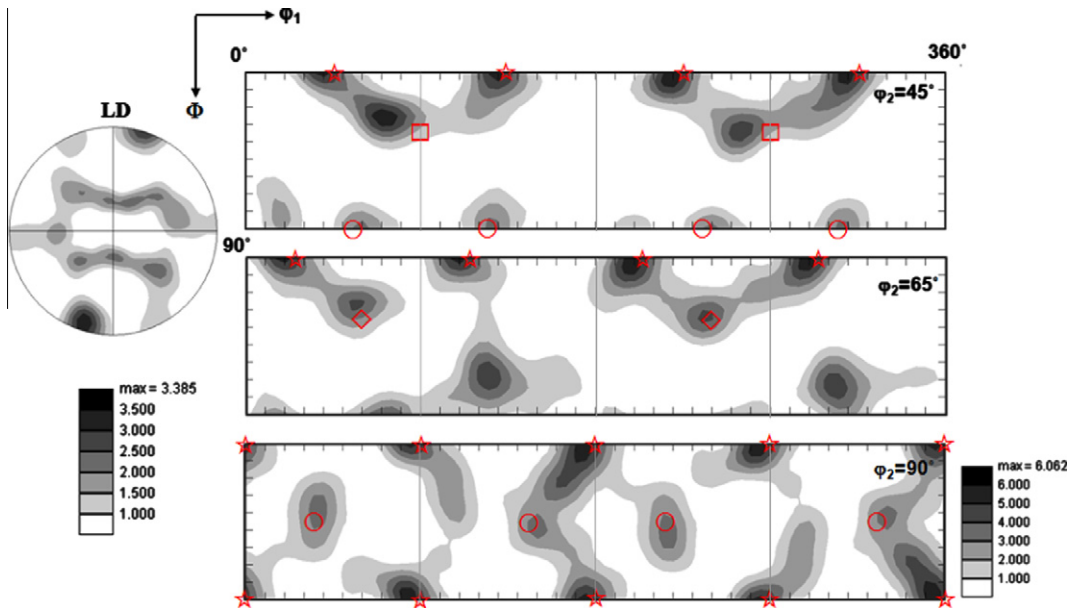


Fig. 21. (1 1 1) Pole figures and ϕ_2 sections of ODF of deformed specimens after deformation ($\gamma/\sqrt{3} = 20\%$) under simple shear loading along the RD at a strain rate of 10^0 s^{-1} and room temperature.

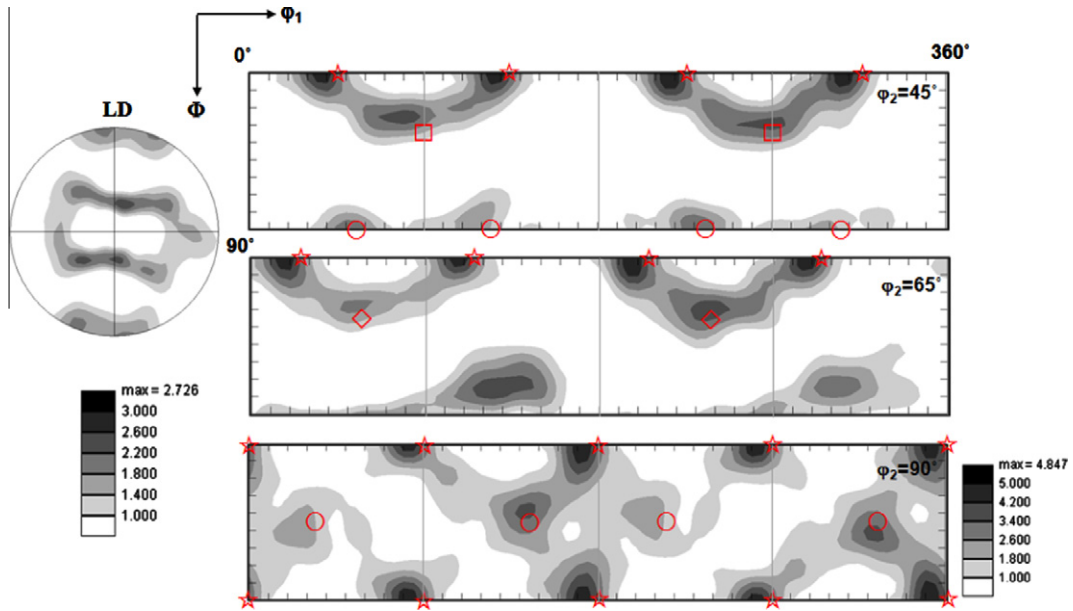


Fig. 22. (1 1 1) Pole figures and φ_2 sections of ODF of deformed specimens after deformation ($\gamma/\sqrt{3} = 20\%$) under simple shear loading along the RD at a strain rate of 10^{-4} s^{-1} and $232 \text{ }^\circ\text{C}$.

initial texture components in the LD//TD specimen. Texture analysis on the ODF sections indicated that the Copper component was relatively unstable under uniaxial tension, compared with the Brass, S, and Cube components.

Fig. 20 shows the texture of the deformed specimen oriented along the RD after simple shear deformation at a strain rate of 10^{-4} s^{-1} and room temperature, as measured using the EBSD technique. Texture analysis on the ODF sections indicated that the Copper component was relatively unstable under simple shear deformation, compared to the Brass, S, and Cube components. It should be noted that the LD//RD specimen exhibited triclinic sample symmetry, during which φ_1 should have expanded to 360° . Fig. 21 shows the texture of the LD//RD specimen deformed by simple shear deformation at a strain rate of 10^0 s^{-1} and room temperature. It was clear from the (1 1 1) pole figure and ODF sections that there was little change in texture with strain rate at room temperature. Although not shown in the present paper, similar dependency of the strain rate

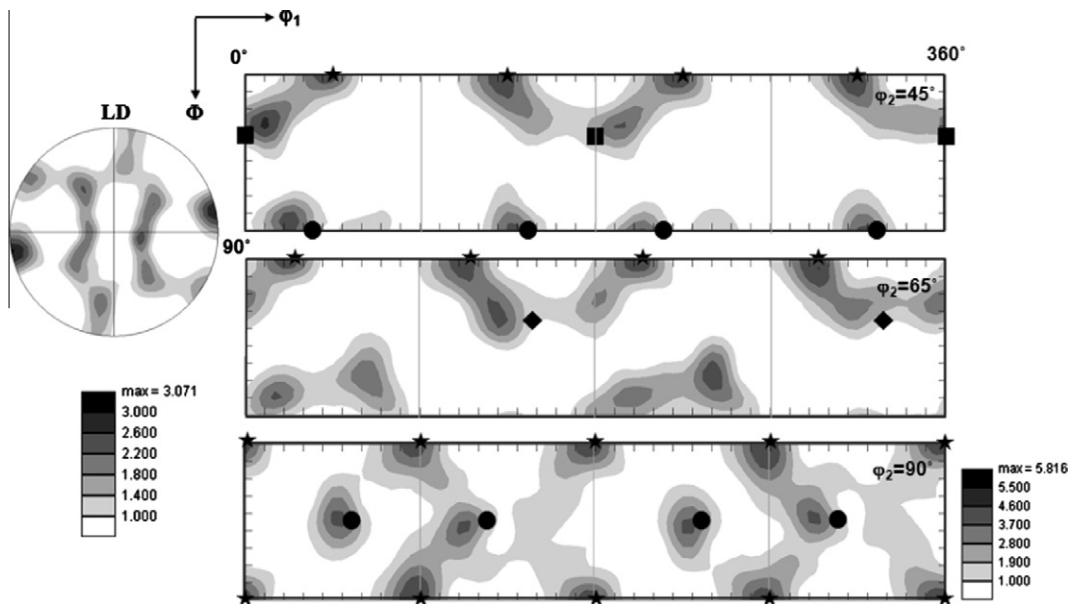


Fig. 23. (1 1 1) Pole figures and φ_2 sections of ODF of deformed specimens after deformation ($\gamma/\sqrt{3} = 20\%$) under simple shear loading along the TD at a strain rate of 10^0 s^{-1} and room temperature.

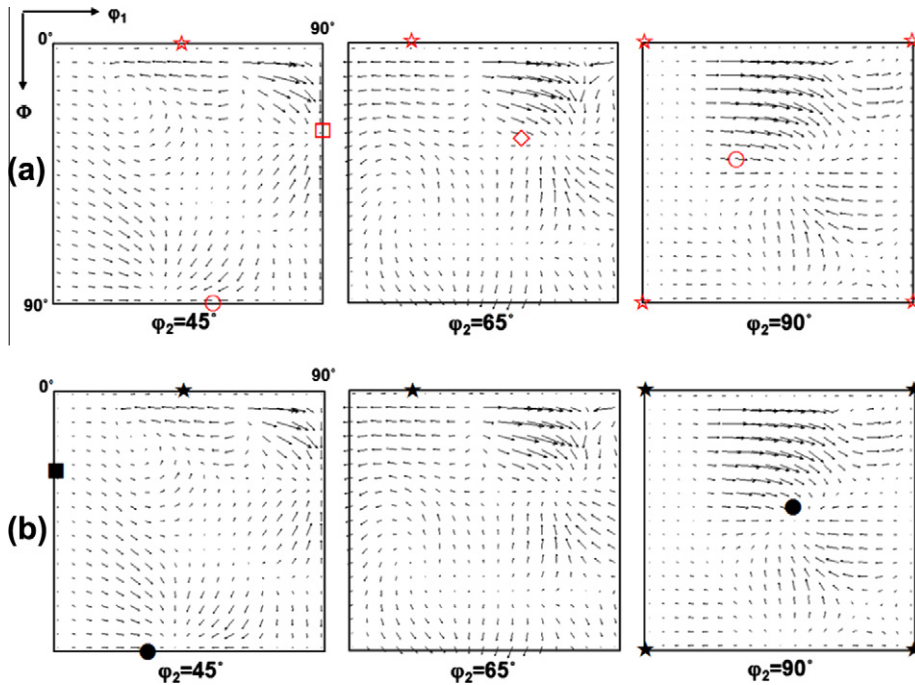


Fig. 24. Rotation rate fields on the φ_2 ODF sections under uniaxial tension: (a) LD//RD and (b) LD//TD.

was observed in the specimens oriented along DD (LD//DD) and the specimens oriented along TD (LD//TD) after simple shear deformation. Fig. 22 shows the texture of the LD//RD specimen deformed by simple shear deformation at a strain rate of 10^{-4} s^{-1} and $232 \text{ }^\circ\text{C}$. A comparison between Fig. 20 and Fig. 22 reveals that a temperature increase from room temperature to $232 \text{ }^\circ\text{C}$ did not significantly affect the texture evolution in the LD//RD specimen during simple shear deformation. Fig. 23 shows the texture of the LD//TD specimen deformed by simple shear deformation at a strain rate of 10^0 s^{-1} and room temperature. Texture analysis on the ODF sections indicated that the S component was relatively unstable under simple shear deformation, compared with the Brass, Copper, and Cube components.

4.3.2. Numerical verification

In order to evaluate the orientation stability of the initial texture components in the AA5754 sheets, rotation rate maps for uniaxial tension and simple shear deformation were calculated using a rate-sensitive polycrystal model, as explained in Section 3.1.

Fig. 24 shows the rotation rate fields on the φ_2 ODF sections under uniaxial tension. The direction of the arrows represents the change in crystallographic orientation, and the arrow length represents the total rotation rate. The stable orientation is that at which all arrow directions converge. To evaluate the orientation stability of the crystallographic orientation, the convergence and stability parameters were calculated using the rate-sensitive polycrystal model, as mentioned in Section 3.1. In the present study, four initial texture components (Brass, Copper, S, Cube) of the AA5754 sheet were selected to compare the kinematic stability under uniaxial tension. Table 2(a) shows the rotation rate, gradient, divergence, and relative stability of the four texture components in the LD//RD specimen under uniaxial tension. Based on $\text{div } \dot{g}$ and Q , the Copper component in the LD//RD specimens was kinematically stable under uniaxial tension. These two parameters explain why the initial orientation of the Copper component in the LD//RD specimens were relatively stable during uniaxial tension, as shown in Figs. 18 and 19. Based on only $\text{div } \dot{g}$, the Brass and S texture components in the LD//RD specimen were kinematically stable under uniaxial tension. A relatively low value of Q explains the low orientation stability of the Brass and S texture components, as shown in Figs. 18 and 19. However, a relatively low absolute value of $\text{div } \dot{g}$ cannot explain why the Cube component was kinematically stable, as shown in Figs. 18 and 19. Table 2(b) shows the rotation rate, gradient, divergence and relative stability of the four texture components in the LD//TD specimens under uniaxial tension. Based on only $\text{div } \dot{g}$, the Copper texture component in the LD//TD specimen was kinematically unstable under uniaxial tension. However, a relatively high value of Q cannot explain why the initial orientation of the Copper component in the LD//TD specimen was kinematically unstable, as shown in Fig. 19(b). It should be noted that the kinematic stability of the four texture components was evaluated by the rate-sensitive polycrystal model, which violates the stress equilibrium condition between grains. The VPSC polycrystal model can be used to overcome this problem of the Taylor model, as explained in Section 3.2. This model assumes a homogenization scheme in which the grain interactions with the matrix are taken into account.

To simulate the texture evolution in the AA5754 sheets deformed at a strain rate of 10^0 s^{-1} and room temperature, the velocity gradient tensor for uniaxial tension was imposed on the VPSC polycrystal model. The ODF, measured using the

Table 2

Rotation rate, gradient, divergence and relative stability of the four texture components in the (a) LD//RD and (b) LD//TD specimens under uniaxial tension.

	Brass	Copper	S	Cube		Brass	Copper	S	Cube
$\dot{\Phi}_1$	-0.01	-1.0	-0.2	-0.49	$\dot{\Phi}_1$	-0.99	0.0	-0.8	-0.51
$\dot{\Phi}$	0.0	0.0	0.08	0.0	$\dot{\Phi}$	0.0	0.0	-0.08	0.0
$\dot{\Phi}_2$	0.0	0.0	-0.19	-0.01	$\dot{\Phi}_2$	0.0	-0.01	0.19	0.01
$\partial\dot{\Phi}_1/\partial\varphi_1$	-0.51	-1.95	-2.89	9.34	$\partial\dot{\Phi}_1/\partial\varphi_1$	0.51	1.96	2.8	10.9
$\partial\dot{\Phi}/\partial\Phi$	0.96	0.21	0.2	-0.63	$\partial\dot{\Phi}/\partial\Phi$	-0.96	-0.11	-0.03	0.64
$\partial\dot{\Phi}_2/\partial\varphi_2$	-2.02	2.29	3.2	-3.72	$\partial\dot{\Phi}_2/\partial\varphi_2$	2.03	-2.31	-2.13	-1.11
divg	-1.58	0.55	0.51	5	divg	1.58	-0.45	0.63	10.43
Q	4.02	-0.55	0.40	0.14	Q	-0.55	3.88	-0.14	0.14

(a) (b)

neutron diffraction technique, was used to generate a set of 5000-grain orientations for VPSC polycrystal modeling. Fig. 25(a) shows the simulation results in the form of the (1 1 1) pole figure and φ_2 sections of the ODF for the LD//RD specimen. It should be noted that the simulation result was similar to the texture measured experimentally, as shown in Fig. 18(b). The VPSC polycrystal model simulated the relatively high orientation stability of the Copper and Cube texture components in the LD//RD specimens during uniaxial tension. Fig. 25(b) shows the simulation results in the form of the (1 1 1) pole figure and φ_2 sections of the ODF for the LD//TD specimen. The simulation results were similar to the texture measured experimentally, as shown in Fig. 19(b). The VPSC polycrystal model successfully simulated the low orientation stability of the Copper component in the LD//TD specimens during uniaxial tension.

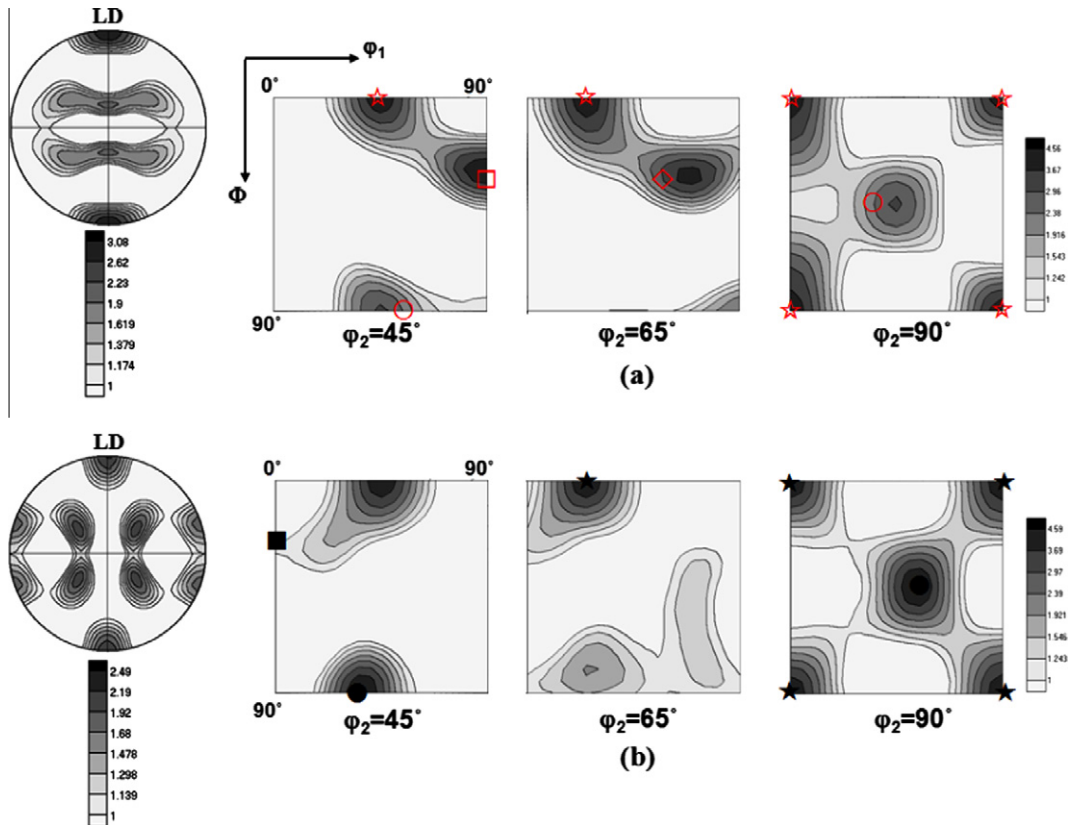


Fig. 25. (1 1 1) pole figure and φ_2 sections of the ODF illustrating deformation textures simulated using VPSC polycrystal model: (a) LD//RD specimen and (b) LD//TD specimen under uniaxial tension.

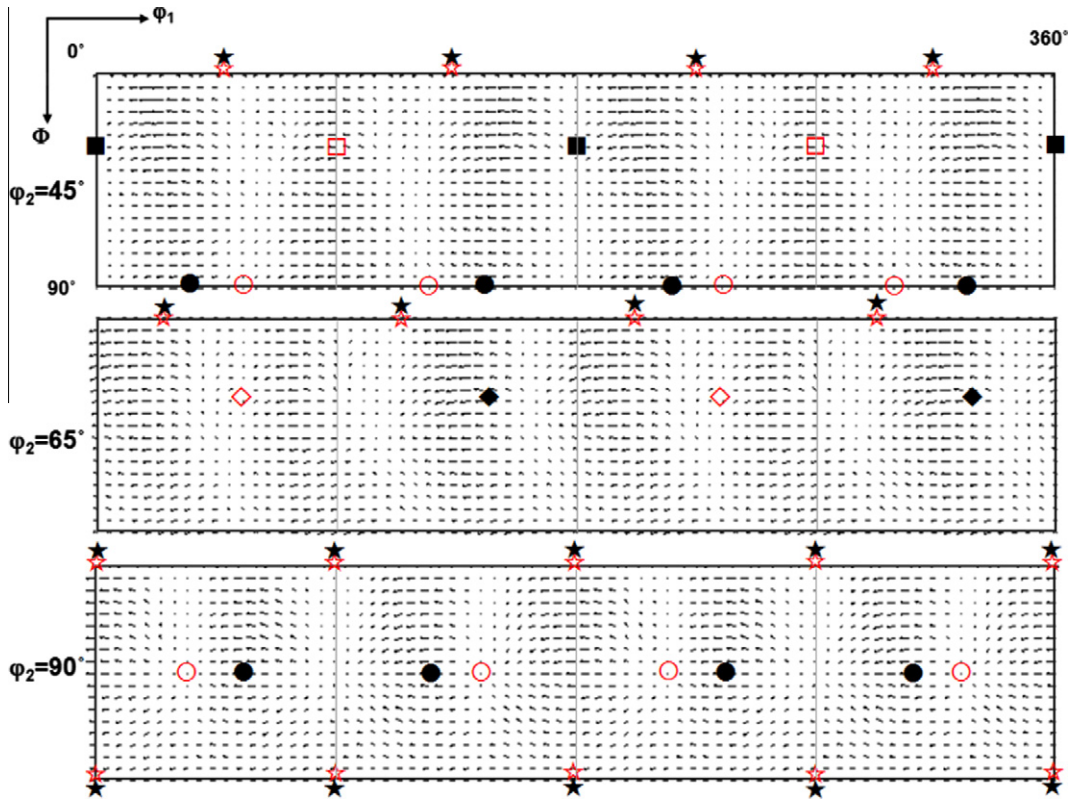


Fig. 26. Rotation rate fields on the φ_2 ODF sections under simple shear deformation.

Fig. 26 shows the rotation rate fields on the φ_2 ODF sections under simple shear deformation. Under simple shear deformation, no stable orientation could be found for the φ_2 ODF sections. To evaluate the orientation stability of the crystallographic orientation, the convergence and stability parameters were calculated using the rate-sensitive polycrystal model, as mentioned in Section 3.1. Table 3(a) shows the rotation rate, gradient, divergence and relative stability of the four texture components in the LD//RD specimen under simple shear deformation. Based on $\text{div } \dot{g}$ and Q , the Copper component in the LD//RD specimens was kinematically unstable under simple shear deformation. The low value of Q explains the low orientation stability of the Brass texture component under simple shear deformation. These two parameters successfully explain why the initial orientation of the Copper component in the LD//RD specimens rotated to the negative φ_1 direction on the $\varphi_2 = 45^\circ$ ODF section during simple shear deformation, as shown in Figs. 20–22. Table 3(b) shows the rotation rate, gradient,

Table 3

Rotation rate, gradient, divergence, and relative stability of the four texture components in the (a) LD//RD and (b) LD//TD specimens under simple shear deformation.

	Brass	Copper	S	Cube
$\dot{\varphi}_1$	-0.49	0.0	0.18	-0.88
$\dot{\Phi}$	0.0	-0.14	-0.13	-0.07
$\dot{\varphi}_2$	0.0	0.0	0.36	0.89
$\partial\dot{\varphi}_1/\partial\varphi_1$	-0.52	-3.71	0.04	0.05
$\partial\dot{\Phi}/\partial\Phi$	-3.74	-1.65	-1.26	-0.51
$\partial\dot{\varphi}_2/\partial\varphi_2$	-1.0	1.33	-3.18	-1.31
div \dot{g}	-5.25	-4.03	-4.41	-1.77
Q	0.73	1.94	0.64	2.22

(a)

	Brass	Copper	S	Cube
$\dot{\varphi}_1$	-0.18	0.0	0.15	-0.9
$\dot{\Phi}$	0.0	0.04	-0.15	-0.07
$\dot{\varphi}_2$	0.0	0.0	0.37	0.91
$\partial\dot{\varphi}_1/\partial\varphi_1$	-1.36	1.45	0.28	-0.21
$\partial\dot{\Phi}/\partial\Phi$	1.38	0.14	-0.36	-1.01
$\partial\dot{\varphi}_2/\partial\varphi_2$	-1.56	3.81	-2.07	-1.18
div \dot{g}	-4.3	5.40	-2.15	-2.39
Q	1.7	3.03	0.66	2.21

(b)

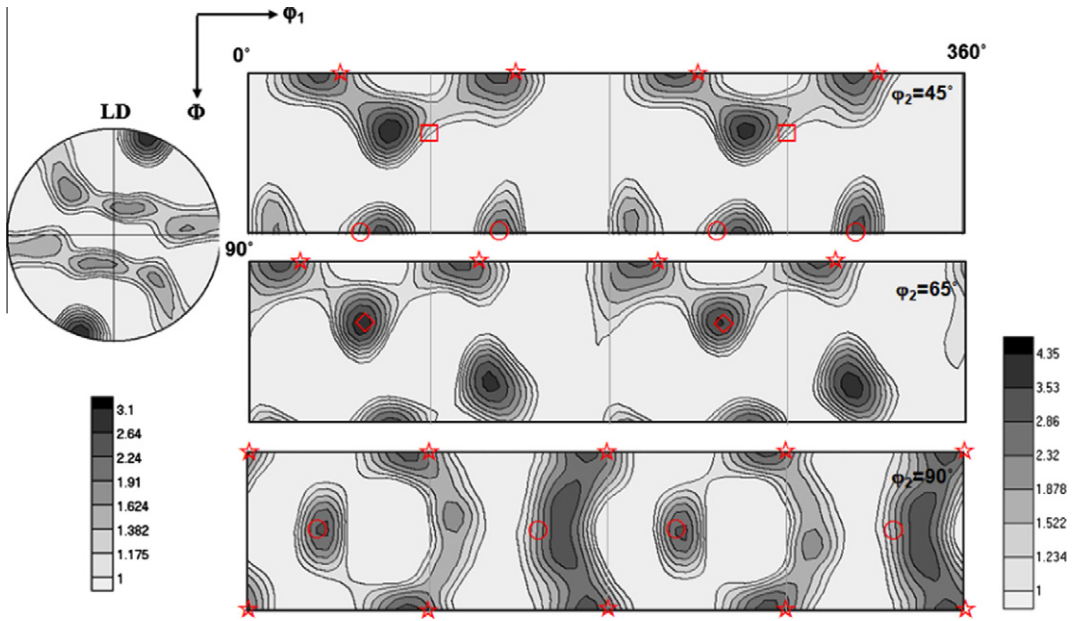


Fig. 27. (1 1 1) pole figure and φ_2 sections of the ODF illustrating deformation textures simulated using VPSC polycrystal model: LD//RD specimen under simple shear deformation.

divergence, and relative stability of the four texture components in the LD//TD specimens under simple shear deformation. Based on only Q , the Copper component in the LD//TD specimen was relatively stable under simple shear deformation compared to the other components. However, the relatively low absolute value of $\text{div } \dot{g}$ partly explains the relatively low orientation stability of the Copper component in the LD//TD specimen, as shown in Fig. 23. Based on $\text{div } \dot{g}$ and Q , the Cube component in the LD//TD specimens was kinematically unstable under simple shear deformation. These two parameters appear to be insufficient to explain why the initial orientation of the Cube component in the LD//TD specimen showed a relatively high orientation stability during simple shear deformation, as shown in Fig. 23.

To simulate the texture evolution in the AA5754 sheets deformed at a strain rate of 10^0 s^{-1} and room temperature, the velocity gradient tensor for simple shear deformation was imposed on the VPSC polycrystal model. Fig. 27 shows the simulation results in the form of the (1 1 1) pole figure and φ_2 sections of the ODF for the LD//RD specimen. It should be noted

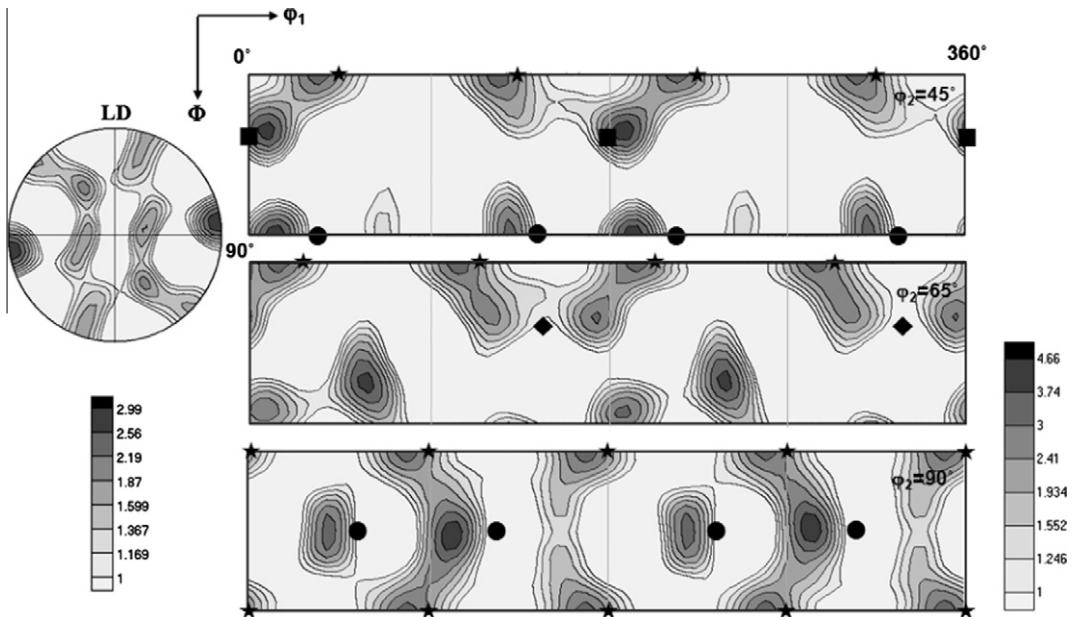


Fig. 28. (1 1 1) pole figure and φ_2 sections of the ODF illustrating deformation textures simulated using VPSC polycrystal model: LD//TD specimen under simple shear deformation.

that the simulation result was similar to the texture measured experimentally, as shown in Fig. 21. The VPSC polycrystal model successfully simulated the rotation of the Copper component in the LD//RD specimens to the negative φ_1 direction during simple shear deformation. Fig. 28 shows the simulation results in the form of the (1 1 1) pole figure and φ_2 sections of the ODF for the LD//TD specimen. The simulation results were similar to the texture measured experimentally, as shown in Fig. 23. The VPSC polycrystal model successfully simulated the low orientation stability of the S component in the LD//TD specimens during simple shear deformation.

5. Conclusions

The results presented in this study included comprehensive stress–strain responses and post-failure texture results for AA5754 sheets at different strain rates and temperatures in through-thickness and in-plane directions. The material showed negative strain rate sensitivity (SRS) at room temperature and a positive strain rate sensitivity at more than 150 °C. The transition temperature of SRS was significantly dependent on the loading direction under simple shear loading. The yield and flow stress for ND compression specimens followed a trend similar to that of in-plane DD compression specimens at all strain rates and temperatures. The temperature sensitivity of the material increased with strain rate and was attributed to dynamic recovery. The (1 1 1) pole figure and ODF sections show that the initial texture components in the AA5754 sheet can be characterized as Brass, Copper, S, and Cube texture components. There was little change in texture with changes in strain rate and temperature during uniaxial tension and simple shear deformation. However, loading direction strongly affected the evolution of deformation texture during uniaxial tension and simple shear deformation. The orientation stability parameters, determined by the rate-sensitive polycrystal model, partially failed to explain the kinematic stability of the initial texture components in AA5754 sheets during uniaxial tension and simple shear deformation. However, the VPSC polycrystal model successfully simulated the evolution of the initial texture components in AA5754 sheets during uniaxial tension and simple shear deformation.

Acknowledgements and Disclaimer

The financial support for this research from GMC through Dr. Raj Mishra is sincerely appreciated. Certain commercial firms and trade names are identified in this report in order to adequately specify aspects of the experimental procedure. Such identification is not intended to imply recommendation or endorsement by the National Institute of Standards and Technology, nor is it intended to imply that the materials or equipment identified are necessarily the best available for the purpose.

References

- Abedrabbo, N., Pourboghraat, F., Carsley, J., 2007. Forming of AA5182-O and AA5754-O at elevated temperatures using coupled thermo-mechanical finite element models. *Int. J. Plasticity* 23, 841–875.
- Arzaghi, M., Beausir, B., Tóth, L.S., 2009. Contribution of non-octahedral slip to texture evolution of fcc polycrystals in simple shear. *Acta Mater.* 57, 2440–2453.
- Banovic, S.W., Iadicola, M.A., Foecke, T., 2008. Textural development of AA 5754 sheet deformed under in-plane biaxial tension. *Metall. Mat. Trans. A* 39, 2246–2258.
- Boger, R.K., Wagoner, R.H., Barlat, F., Lee, M.G., Chung, K., 2005. Continuous, large strain, tension/compression testing of sheet material. *Int. J. Plasticity* 21, 2319–2343.
- Bouvier, S., Gardey, B., Haddadi, H., Teodosiu, C., 2006a. Characterization of the strain-induced plastic anisotropy of rolled sheets by using sequences of simple shear and uniaxial tensile tests. *J. Mat. Proc. Tech.* 174, 115–126.
- Bouvier, S., Haddadi, H., Levée, P., Teodosiu, C., 2006b. Simple shear tests: experimental techniques and characterization of the plastic anisotropy of rolled sheets at large strains. *J. Mat. Proc. Tech.* 172, 96–103.
- Brahme, A.P., Inal, K., Mishra, R.K., Saimoto, S., 2011. The backstress effect of evolving deformation boundaries in FCC polycrystals. *Int. J. Plasticity* 27, 1252–1266.
- Brand, P.C., Prask, H.J., Herold, T.G., 1997. Residual stress measurements at the NIST reactor. *Physica B: Condensed Matter*. 241–243, 1244–1245.
- Burger, G.B., Gupta, A.K., Jeffrey, P.W., Lloyd, D.J., 1995. Microstructural control of aluminum sheet used in automotive applications. *Mat. Charc.* 35, 23–39.
- Choi, S.-H., Cho, J.H., Oh, K.H., Chung, K., Barlat, F., 2000a. Texture evolution of FCC sheet metals during deep drawing process. *Int. J. Mech. Sci.* 42, 1571–1592.
- Choi, S.-H., Brem, J.C., Oh, K.H., Barlat, F., 2000b. Macroscopic anisotropy in AA5019A sheet. *Acta Mater.* 48, 1853–1863.
- Choi, S.-H., Han, S.H., Chin, K.G., 2009. Simulation of orientation gradients in a ferrite matrix containing hard martensite under plane-strain flange deformation. *Acta Mater.* 57, 1947–1958.
- Choi, S.-H., Shin, E.J., Seong, B.S., 2007. Simulation of deformation twins and deformation texture in an AZ31 Mg alloy under uniaxial compression. *Acta Mater.* 55, 4181–4192.
- Clausen, A.H., Børvik, T., Hopperstad, O.S., Benallal, A., 2004. Flow and fracture characteristics of aluminium alloy AA5083–H116 as function of strain rate, temperature and triaxiality. *Mat. Sci. Engg. A* 364, 260–272.
- Cole, G.S., Sherman, A.M., 1995. Light weight materials for automotive applications. *Mat. Char.* 35, 3–9.
- Ghavam, K., Naghdabadi, R., 2011. Constitutive modeling of temperature and strain rate dependent elastoplastic hardening materials using a corotational rate associated with the plastic deformation. *Int. J. Plasticity* 27, 1445–1455.
- Hadianfard, M.J., Smerd, R., Winkler, S., Worswick, M., 2008. Effects of strain rate on mechanical properties and failure mechanism of structural Al–Mg alloys. *Mat. Sci. Engg. A* 492, 283–292.
- Hamelin, C.J., Diak, B.J., Pilkey, A.K., 2011. Multiscale modelling of the induced plastic anisotropy in bcc metals. *Int. J. Plasticity* 27, 1185–1202.
- Hance, B.M., 2005. Influence of discontinuous yielding on normal anisotropy (r -value) measurements. *J. Mat. Eng. Performance* 14, 616–622.
- Iadicola, M.A., Foecke, T., Banovic, S.W., 2008. Experimental observations of evolving yield loci in biaxially strained AA5754-O. *Int. J. Plasticity* 24, 2084–2101.
- Kalidindi, S.R., Bronkhorst, C.A., Anand, L., 1992. Crystallographic texture evolution in bulk deformation processing of fcc metals. *J. Mech. Phys. Solids*. 40, 537–569.

- Kang, J., Wilkinson, D.S., Jain, M., Embury, J.D., Beaudoin, A.J., Kim, S., Mishra, R., Sachdev, A.K., 2006. On the sequence of inhomogeneous deformation processes occurring during tensile deformation of strip cast AA5754. *Acta Mater.* 54, 209–218.
- Khan A.S., Liu H., 2012. Variable strain rate sensitivity in an aluminum alloy: Response and constitutive modeling. *Int. J. Plasticity* 36, 1–4.
- Khan, A.S., Pandey, A., Gnäupel-Herold, T., Mishra, R.K., 2011. Mechanical response and texture evolution of AZ31 alloy at large strains for different strain rates and temperatures. *Int. J. Plasticity* 27, 688–706.
- Khan, A.S., Baig, M., 2011. Anisotropic responses, constitutive modeling and the effects of strain-rate and temperature on the formability of an aluminum alloy. *Int. J. Plasticity* 27, 522–538.
- Khan, A.S., Kazmi, R., Pandey, A., Stoughton, T., 2009. Evolution of subsequent yield surfaces and elastic constants with finite plastic deformation. Part I: a very low work hardening aluminum alloy: Al-6061–T 6511. *Int. J. Plasticity* 25, 1611–1625.
- Khan, A.S., Pandey, A., Stoughton, T., 2010a. Evolution of subsequent yield surfaces and elastic constants with finite plastic deformation. Part II: a very high work hardening aluminum alloy (annealed 1100 Al). *Int. J. Plasticity* 26, 1421–1431.
- Khan, A.S., Pandey, A., Stoughton, T., 2010b. Evolution of subsequent yield surfaces and elastic constants with finite plastic deformation, part-III: Yield surface in tension–tension stress space (Al 6061-T 6511 & annealed 1100 Al). *Int. J. Plasticity* 26, 1432–1441.
- Khan, A.S., Suh, Y.S., Kazmi, R., 2004. Quasi-static and dynamic loading responses and constitutive modeling of titanium alloys. *Int. J. Plasticity* 20, 2233–2248.
- Li, D., Ghosh, A., 2003. Tensile deformation behavior of aluminum alloys at warm forming temperatures. *Mat. Sci. Engg. A* 352, 279–286.
- Li, S., 2008. Orientation stability in equal channel angular extrusion. Part I: Face-centered cubic and body-centered cubic materials. *Acta Mater.* 56, 1018–1030.
- Lou, X.Y., Li, M., Boger, R.K., Agnew, S.R., Wagoner, R.H., 2007. Hardening evolution of AZ31B Mg sheet. *Int. J. Plasticity* 23, 44–86.
- Luo, M., Dunand, M., Mohr, D., 2012. Experiments and modeling of anisotropic aluminum extrusions under multi-axial loading – Part II: Ductile fracture. *Int. J. Plasticity* 32–33, 36–58.
- Molinari, A., Canova, G., Ahzi, A., 1987. A self consistent approach of the large deformation polycrystal viscoplasticity. *Acta Metallurgica* 35, 2983–2994.
- Naka, T., Yoshida, F., 1999. Deep drawability of type 5083 aluminium–magnesium alloy sheet under various conditions of temperature and forming speed. *J. Mat. Proce. Tech.* 89–90, 19–23.
- Park, D.-Y., Niewczas, M., 2008a. Plastic deformation of Al and AA5754 between 4.2 K and 295 K. *Mat. Sci. Engg. A* 491, 88–102.
- Park, D.-Y., Niewczas, M., 2008b. Texture evolution in AA5754 alloys deformed in tension. *Mat. Sci. Engg. A* 497, 65–73.
- Picu, R.C., Vincze, G., Ozturk, F., Gracio, J.J., Barlat, F., Maniatty, A.M., 2005. Strain rate sensitivity of the commercial aluminum alloy AA5182-O. *Mat. Sci. Engg. A* 390, 334–343.
- Sarkar, J., Kutty, T.R.G., Conlon, K.T., Wilkinson, D.S., Embury, J.D., Lloyd, D.J., 2001. Tensile and bending properties of AA5754 aluminum alloys. *Mat. Sci. Engg. A* 316, 52–59.
- Smerd, R., Winkler, S., Salisbury, C., Worswick, M., Lloyd, D., Finn, M., 2005. High strain rate tensile testing of automotive aluminum alloy sheet. *Int. J. Impact Engg.* 32, 541–560.
- Sung J.H., Kim J. H., Wagoner R.H., 2010. A plastic constitutive equation incorporating strain, strain-rate, and temperature. *Int. J. Plasticity* 26, 1746–1771.
- Tozawa, N., 1978. Plastic deformation behavior under the conditions of combined stress. In: Koistinen, D.P., Wang, N.M. (Eds.), *Mechanics of Sheet Metal Forming*. Plenum Press, New-York, pp. 81–110.
- Wagenhofer, M., Natishan, M.E., Armstrong, R.W., Zerilli F.J., 1999. Influences of strain rate and grain size on yield and serrated flow in commercial Al-Mg alloy 5086. *Scripta Mater.* 41, 1177–1184.
- Wen, W., Morris, J.G., 2003. An investigation of serrated yielding in 5000 series aluminum alloys. *Mat. Sci. Engg. A* 354, 279–285.
- Yoon J.W., Barlat F., Gracio J.J., Rauch E., 2005. Anisotropic strain hardening behavior in simple shear for cube textured aluminum alloy sheets. *Int. J. Plasticity* 12, 2426–2447.